博士論文

Morphogenesis of Influenza Virus Particle

(インフルエンザウイルスの粒子形成機構)

杉田　征彦

CONTENTS

PREFACE

Viruses are tiny infectious organisms that are occasionally pathogenic to the hosts they depend on to reproduce (Fig. 1). Once viruses enter host cells, the viral genome is generally transcribed into mRNAs, which are translated into viral proteins by using host metabolic and transcription/translation machinery. At the same time, the viral genome is replicated by using both host cellular machinery as well as viral proteins such as the viral polymerases. Then, the newly synthesized viral genome and proteins are finally assembled into progeny virions. These virions take various forms such as regular icosahedral, spherical, elliptical, and filamentous shapes with or without lipid envelopes derived from host cell membranes. The specific morphologies of these viruses appear to be optimized to protect and maintain their genome. Therefore, viral morphological features have long been extensively investigated not only to further our understanding of viral pathogenesis, but also to assist in the diagnosis of viral diseases by transmission electron microscopy.

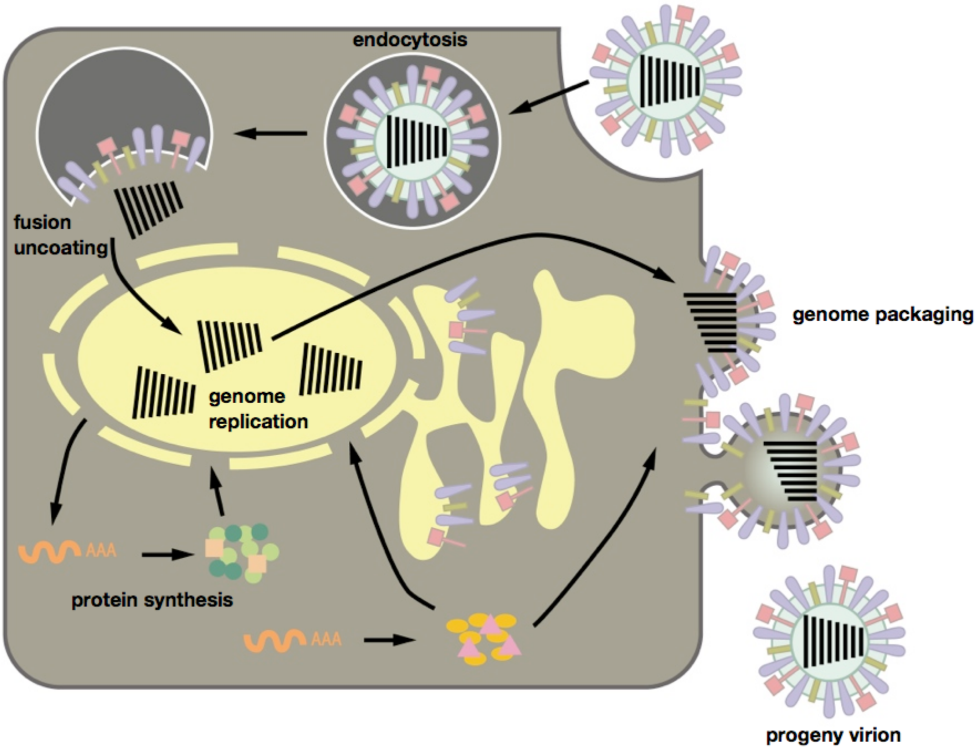

Figure 1. A Schematic diagram of influenza viral replication cycle. Influenza virus attaches to the cellular membranes via host sialic acid receptors and is internalized by endocytosis. The viral envelope fuses with endosome membranes in a pH-dependent manner. Then the genome is uncoated and released into the cytoplasm. The genome is replicated in nucleus and viral proteins are synthesized. Finally, viral proteins are assembled, and the viral genome is packaged into the progeny virion.

Influenza A virus, a member of the *Orthomyxoviridae*, is an enveloped virus with an eight-segmented, negative-sense, single-stranded RNA genome (Fig. 2). When influenza virions are observed by using negative-staining electron microscopy, they often appear as spherical, elliptical, filamentous, or sometimes irregular shapes, which is referred to as pleomorphism. Inside the virion, each viral genomic RNA segment forms a ribonucleoprotein complex (RNP) together with viral nucleoproteins and the heterotrimeric RNA-dependent RNA polymerase complex. Recent electron microscopic studies have shown that eight RNPs are arranged in a specific array, with seven RNPs surrounding a central one, and are selectively packaged into the virion, underneath its budding tip. Extensive research on the polymorphic outer features of the virions and on the RNP architecture inside the virions has been conducted; however, the morphogenesis of influenza virions is not yet fully understood.

By using various electron microscopic techniques, I have studied the interior and exterior morphologies of influenza virions. In Chapter I, to clarify the native morphology of the influenza virion, I attempted to determine whether the irregular-

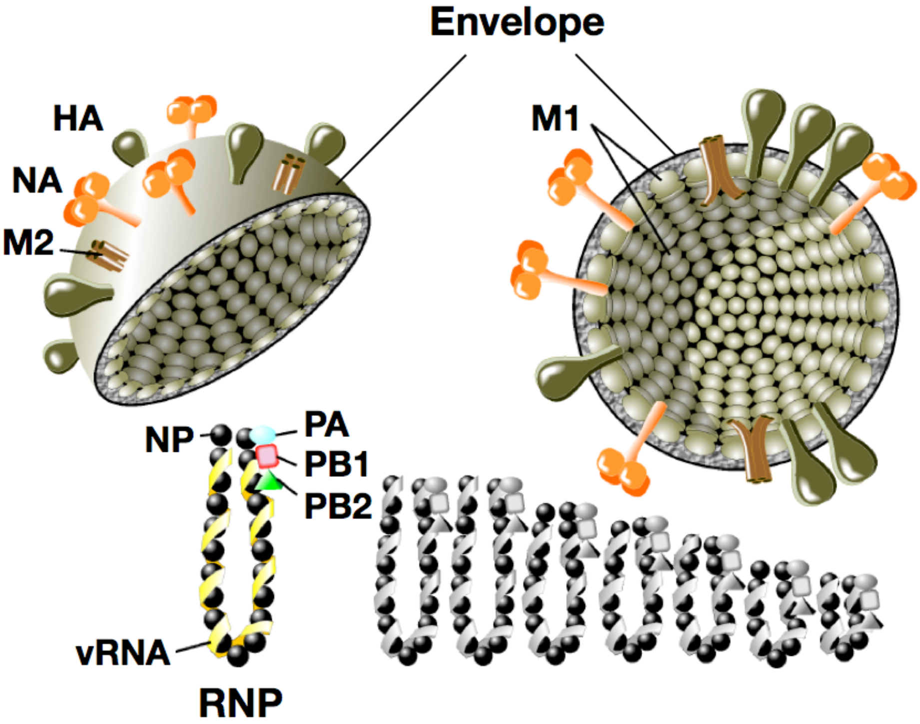

Figure 2. A Schematic diagram of virion structure. The virion possesses many membrane-spanning glycoproteins, haemagglutinin (HA) and neuraminidase (NA), and small amounts of an ion channel protein (M2) on their surface. The membrane protein (M1), which binds to the lipid envelope, is thought to maintain virion structure. The eight-segmented genomic RNA (vRNA) is associated with multiple copies of nucleoproteins (NPs) and the heterotrimeric RNA-dependent RNA polymerase complexes that comprise PA, PB1, and PB2, which together form the ribonucleoprotein complex (RNP).

shaped influenza virion is native and which viral component is important for virion integrity. In Chapter II, I analyzed the orientation of the viral RNPs inside the virion to elucidate the morphogenesis and genome packaging mechanisms of influenza virus.

Chapter I

The Native Morphology of Influenza Virions

I.1 ABSTRACT

It is widely accepted that typical influenza A virions are pleomorphic; they are spherical, elliptical, or filamentous, about 100 nm in diameter, and can sometimes appear irregularly shaped after negative staining. However, these irregular virions have not been observed with ultrathin-section transmission or scanning electron microscopy. In this study, I aimed to determine whether ultracentrifugation, which is routinely used in virus purification before the negative-staining process, affects virion morphology by using chemical fixatives. The morphologies of unfixed, osmium tetroxide (OsO_4)-fixed, or glutaraldehyde (GLA)-fixed virions of A/Puerto Rico/8/34 (PR8; H1N1) strain, whose structures are typically spherical or elliptical, were compared quantitatively before and after ultracentrifugation. The unfixed virions of A/Udorn/307/72 (Udorn; H3N2) strain, which have a filamentous morphology, were also observed by using negative staining before and after ultracentrifugation. When PR8 virions were observed by using ultrathin-section transmission and scanning electron microscopy, they appeared uniformly elliptical or spherical. When observed by negative staining, most PR8 virions

before ultracentrifugation were also spherical or elliptical. However, the morphology of the unfixed PR8 virions was appreciably altered from elliptical to irregular upon ultracentrifugation. By contrast, GLA-fixed PR8 virions remained uniformly elliptical even after ultracentrifugation. The filamentous virions of Udorn strain were similarly greatly deformed after ultracentrifugation. When a virus with an 11-amino acid deletion at the C terminus of its M2 cytoplasmic tail was ultracentrifuged, its morphology was appreciably deformed compared with that of the wild-type virus. These results demonstrate that, in nature, influenza A virions are regularly spherical, elliptical, or filamentous, but ultracentrifugation disrupts this native morphology, and that the cytoplasmic tail of M2 is important for structural integrity of the virion.

I.2 INTRODUCTION

Influenza A virus is an enveloped virus with a segmented, single-strand, negative-sense RNA genome [1]. Its virions are generally spherical or elliptical and about 100 nm in diameter; occasionally, they are filamentous reaching over 20 μm in length, and sometimes they are irregular in shape. They possess many membrane-spanning glycoproteins, hemagglutinin (HA) and neuraminidase (NA), and small amounts of an ion channel protein (M2) on their surface. The matrix protein (M1), which binds to the lipid envelope, is thought to maintain virion structure [1]. Previous studies have shown that single amino acid substitutions in M1 alter the virion morphology from filamentous to spherical, and vice versa [2-4]. Deletion of the cytoplasmic tail of M2, HA, or NA also alters virion morphology from spherical/elliptical to irregular [5, 6]. Thus, the interactions among M1, M2, HA, and NA are important for the formation and preservation of the characteristic virion shapes.

The virion structures of influenza A viruses have been extensively investigated by using various electron microscopies. When observed by ultrathin-section transmission electron microscopy (ultrathin-section TEM) or scanning electron microscopy (SEM), influenza virions appear spherical or elliptical [7-12]. On the other hand, negatively stained influenza virions often show varied morphologies from virion to virion, including irregularly shaped virions [13-17]. This discrepancy could be due to artifacts caused during sample preparation for negative staining, as artifacts can be introduced to fragile biological samples on air drying [18, 19]. However, I cannot exclude other possibilities. In this study, the effects of ultracentrifugation on influenza virion morphology were evaluated as a potential cause of changes in virion morphology, since sample preparation for negative staining often involves ultracentrifugation in order to purify the virions.

I.3 MATERIALS AND METHODS

Viruses

A stock of A/Puerto Rico/8/34 (PR8; H1N1) strain was prepared by growing the virus in the allantoic cavity of 10-day-old chicken embryos at 37 ºC for 2 days.

293T cells were propagated in Dulbecco's modified Eagle's medium containing 10% fetal bovine serum. Madin-Darby canine kidney (MDCK) cells were cultured in minimum essential medium containing 5% newborn calf serum. All cell cultures were supplemented with penicillin-streptomycin solution (x100; Wako Pure Chemical Industries) and maintained at 37°C in an atmosphere of 5% CO_2. A/WSN/33 (WSN; H1N1) wild-type virus and its mutant virus, which had an 11-amino acid deletion from the C-terminus of its M2 cytoplasmic tail (M2Δ11), were generated in 293T cells by using reverse genetics as described previously [5, 20].

Stocks of WSN wild-type, M2Δ11, and A/Udorn/307/72 (Udorn; H3N2) virus were prepared by growing the virus in the MDCK cells at 37 ºC for 2 days.

Fixation and ultracentrifugation

Allantoic fluid or culture supernatant of MDCK cells was centrifuged at 780 x g for 5 min to remove debris. Then aliquots of PR8 virions were fixed with glutaraldehyde (GLA) or osmium tetroxide (OsO_4) at a final concentration of 2.5% or 0.5%, respectively, for 1 h at 4 ºC. Udorn and WSN virions were kept unfixed. The fixed or unfixed samples were ultracentrifuged through a 20% (w/w) sucrose cushion at 90,000 x *g* for 1.5 h at 4 ºC. The pelleted virions were then suspended in phosphate-buffered saline (PBS).

Negative staining

Virions were adsorbed to formvar-coated copper mesh grids, negatively stained with 2% phosphotungstic acid solution and air-dried. Digital images of virions were taken with a TECNAI F20 electron microscope (FEI Company) at 80 or 200 kV.

Ultrathin-section transmission electron microscopy (Ultrathin-section TEM)

At 24 hours after inoculation with PR8 virus, the chorio-allantoic membranes of embryonated chicken eggs were harvested and wash with PBS. MDCK cells were inoculated with WSN wild-type or M2Δ11 virus and incubated at 37 ºC for 24 h. These samples were pre-fixed with 2.5% GLA in 0.1 M cacodylate buffer (pH＝7.4) for 1 h at 4°C. They were then washed with the same buffer and post-fixed with 2% OsO_4 in the same buffer for 1 h at 4°C. After being dehydrated with a series of ethanol gradients followed by propylene oxide, the samples were embedded in Epon 812 Resin mixture (TAAB) and polymerized at 70°C for 2 days. Ultrathin sections, 50-nm thick, were stained with 2% uranyl acetate (UA) in 70% ethanol and Reynolds' lead solution, and examined with a TECNAI F20 electron microscope (FEI Company) at 80 or 200 kV.

Scanning electron microscopy (SEM)

Allantoic membranes were fixed as described for ultrathin-section TEM. The fixed membranes were dehydrated with a series of ethanol gradients, followed by t-butanol, and dried in an ES-2030 freeze dryer (Hitachi High-Technologies Corp.). The specimens were then coated with OsO_4 by using an HPC-1S osmium coater (Vacuum Device Inc.) and examined with an S-4200 microscope (Hitachi High-Technologies Corp.).

Western blotting

Virions, purified by ultracentrifugation through a 20% (w/w) sucrose cushion, were suspended in 2× Tris-Glycine SDS sample buffer (Invitrogen) with or without dithiothreitol at a final concentration of 100 mM and incubated for 5 min at 95°C. The samples were subjected to SDS-PAGE on Tris-Glycine gels (mini-protean TGX gel any kD; Bio-Rad Laboratories), and then transferred to Immobilon-P transfer membranes (Millipore Corporation). The membranes were treated with a commercial blocking buffer (Blocking One; Nacalai Tesque) and incubated with primary antibodies, an anti-influenza virus rabbit polyclonal antibody (R309) or an anti-M2 (14C2) monoclonal antibody, at 4°C overnight. The antibody-antigen complexes were detected by using an immunodetection kit (ABC kit; Vector Laboratories) and Immunostain HRP-1000 (Konica Minolta Medical and Graphic).

Quantification of virion shapes

Around 200 virions, whose lengths were less than 300 nm, were randomly picked for quantification. Their perimeters were traced and their boundary lengths and areas measured by using ImageJ software (http://rsbweb.nih.gov/ij/). The values for shape complexity, which are defined as the ratio of $(\text{perimeter})^2/4\pi(\text{area})$, were calculated as described elsewhere [21]. The complexity value theoretically takes 1.0 for round virions and becomes larger for elongated or distorted virions.

I.4 RESULTS

Budding virions observed by ultrathin-section TEM

When influenza A virions budding from infected cells are observed by ultrathin-section TEM, they are uniformly elliptical or spherical [7, 8, 11, 22, 23]. To confirm whether ultrathin-sectioned virions of PR8 strain are also uniformly elliptical, virions budding from allantoic membrane cells were subjected to ultrathin-section TEM. The virions budding from the apical plasma membranes were elliptical and almost uniform in shape, although they have slightly different lengths (Fig. 3A).

Next, to quantify the shapes of the virions visualized by ultrathin-section TEM, I randomly picked longitudinally sectioned virions containing rod-like ribonucleoprotein (RNP) complexes (Fig. 3B), whose long axes were thought to be entirely present within the ultrathin sections (50-nm thick), likely representing the size and shape of the whole virion. Virions that did not contain any RNPs were excluded, because they were likely sectioned at the edge and would, therefore, not have intact shapes. For descriptive purposes, the shape complexity values, which numerically classify the pleomorphicity

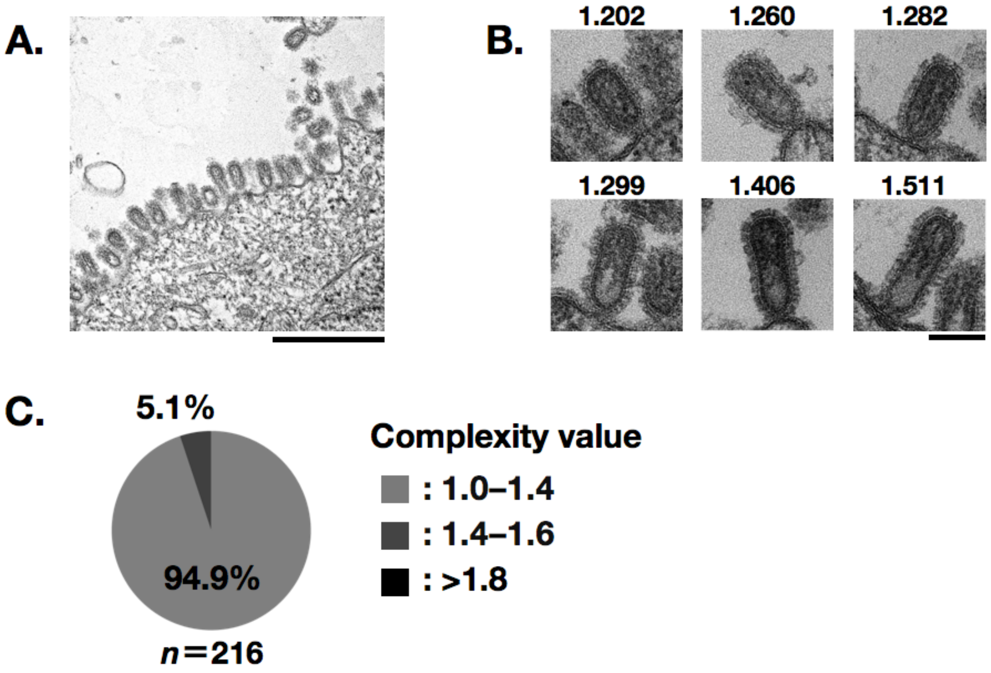

Figure 3. Budding PR8 virions observed by using ultrathin-section TEM. (A) A representative electron micrograph of PR8 virions budding from the cells of allantoic membranes. Uniformly oval virions can be seen budding from the apical plasma membrane. (B) Representative electron micrographs of ultrathin-sectioned virions. Respective shape complexity values are given above the photos. (C) Proportion of shape complexity values of ultrathin-sectioned virions. In total, 216 virions were assessed. Scale bars, 500 nm (A); 100 nm (B).

of virions, were calculated as described in the Materials and Methods and divided into three groups: 1.0 to 1.4, 1.4 to 1.8, and >1.8. In general, the 1.0–1.4 group contained spherical or elliptical particles, the 1.4–1.8 group had elongated or irregular-shaped virions, and the >1.8 group had extremely irregular virions (Fig. 3). Of the ultrathin-sectioned PR8 virions, 94.9% were spherical or elliptical and fell into the 1.0–1.4 group, whereas 5.1% were elongated and classified in the 1.4–1.8 group (Fig. 3B and C). No virion was irregular in shape. My observations indicate that most virions observed by using ultrathin-section TEM are uniform in shape.

Released virions observed by using SEM

Next, I examined virions that were budding and released from the cells of allantoic membranes by using SEM. The virions that budded from these cells were homogenous in shape (Fig. 4A), similar to those observed by using ultrathin-section TEM (Fig. 3A). Released virions bound to chicken erythrocytes were also observed by using SEM (Fig. 4B) and 197 virions, selected at random, were subjected to the morphological measurements. As was the case with ultrathin-section TEM, most of the virions were

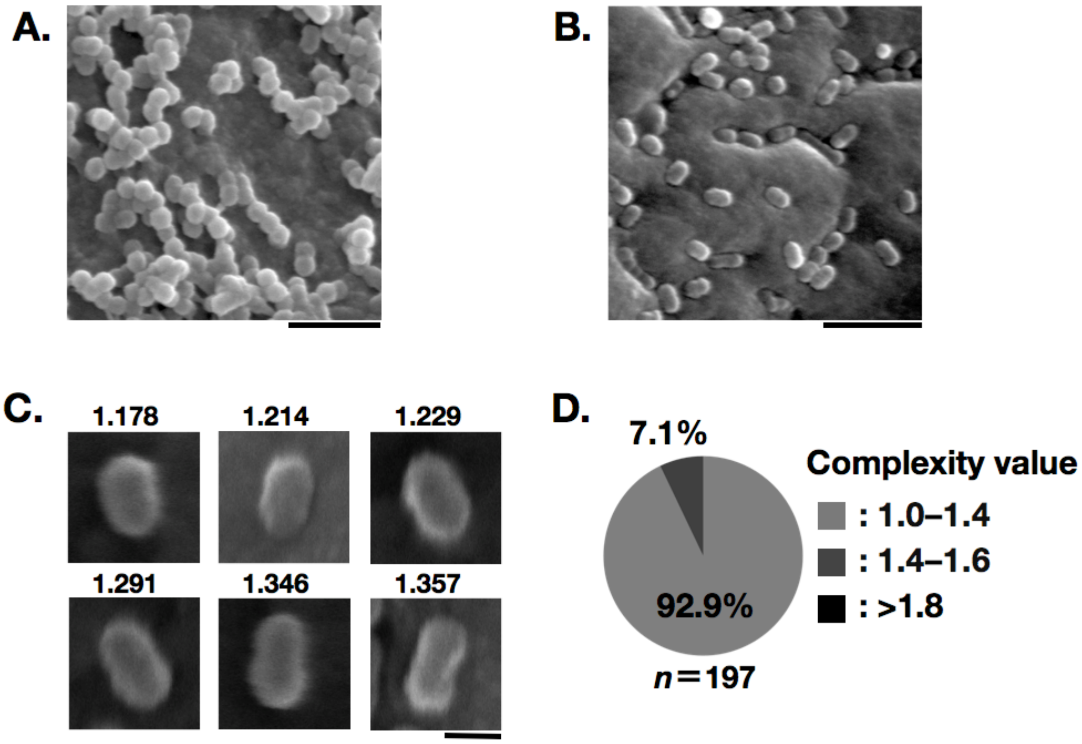

Figure 4. PR8 virions observed by using SEM. (A) A representative electron micrograph of PR8 virions budding from the cells of allantoic membranes. (B) A representative electron micrograph of virions adsorbed onto a chicken erythrocyte, which was found with allantoic membrane cells under a scanning electron microscopic field. Elliptical and spherical virions can be seen. (C) A higher magnification of the representative electron micrographs of released virions on chicken erythrocytes. Respective shape complexity values are given above the photos. (D) Proportion of shape complexity values of virions visualized by using SEM. In total, 197 virions were examined. Scale bars, 500 nm (A and B); 100 nm (C).

round or oval and their complexity values fell into the 1.0–1.4 group (Fig. 4C and D). About 7% of the virions had an elongated shape and were categorized in the 1.4–1.8 group, and no virion was irregular in shape (Fig. 4C and D). These results suggest that most virions observed by using SEM are round or elliptical in shape and are morphologically homogenous.

Negatively stained virions

In earlier reports, negatively stained virions were often heterogeneous and sometimes showed irregular shapes [13-17], which were generally thought to be artifacts introduced during the air-drying step of negative staining [18, 19]. To identify steps other than air-drying that may cause changes in virion morphology, I focused on ultracentrifugation, because it is often performed to purify or concentrate virions before negative staining. To evaluate the effect of ultracentrifugation on virion shape, I prepared virions that were unfixed or fixed with GLA or OsO_4. Subsets of specimens were directly observed by use of negative staining with 2% phosphotungstic acid solution, and the rest were subjected to ultracentrifugation at 90,000 x g for 1.5 h at 4 ºC. In all samples, with or without ultracentrifugation, spike proteins composed of HA and NA were clearly observable on the virion surfaces (Fig. 5A–F). Most of the virions without ultracentrifugation had oval shapes but a small number of morphologically irregular virions were also observed (Fig. 5A and 6A–C). Without ultracentrifugation, about 90% of the virions were classified in the 1.0–1.4 group, while 6%–10% were elongated and classified in the 1.4–1.8 group (Fig. 5A–C and G–I). Some deformed virions that were classified in the >1.8 group were found in the unfixed sample without ultracentrifugation (Fig. 5A, G and 4A–C); similar virions were not observed in the GLA- or OsO_4-fixed samples (Fig. 5B–C and H–I).

Upon ultracentrifugation, unfixed virions showed various irregular amoeba-like shapes (Fig. 5D and 6D-G). A total of 21.3% of them fell into the 1.4–1.8 group and 9.1% were in the >1.8 group (Fig. 5J). Some virions were not only irregular shaped but also enlarged, suggesting that they were fused together. (Fig. 6G) However, virions fixed with GLA prior to ultracentrifugation did not show significant changes in morphology and most had an elongated shape (Fig. 5F and L). Although OsO_4-fixed

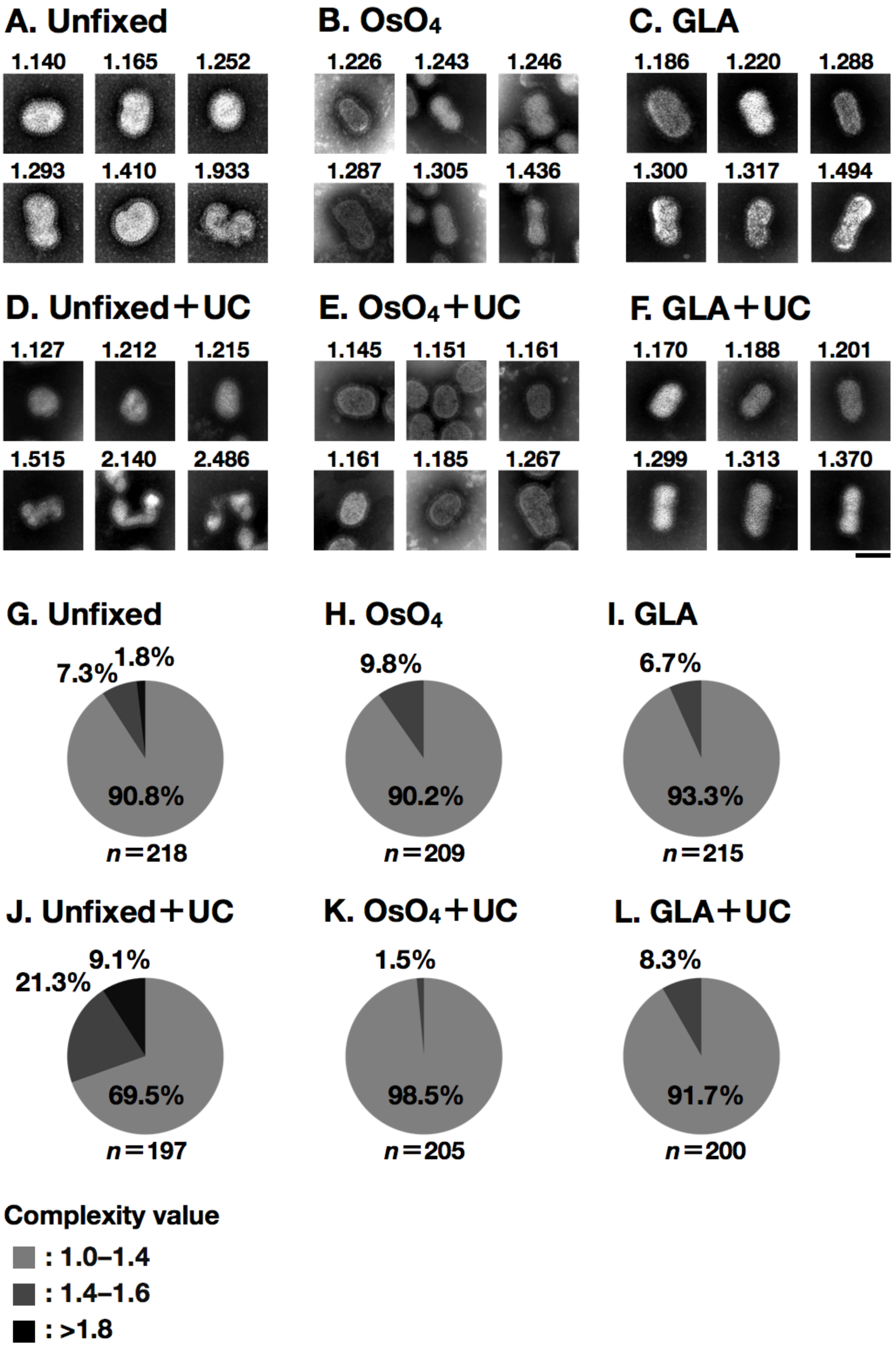
A. Unfixed
1.140
1.165
1.252
1.293
1.410
1.933
B. OsO_4
1.226
1.243
1.246
1.287
1.305
1.436
C. GLA
1.186
1.220
1.288
1.300
1.317
1.494
D. Unfixed+UC
1.127
1.212
1.215
1.515
2.140
2.486
E. OsO_4+UC
1.145
1.151
1.161
1.161
1.185
1.267
F. GLA+UC
1.170
1.188
1.201
1.299
1.313
1.370
G. Unfixed
7.3%
1.8%
90.8%
n=218
H. OsO_4
9.8%
90.2%
n=209
I. GLA
6.7%
93.3%
n=215
J. Unfixed+UC
21.3%
9.1%
69.5%
n=197
K. OsO_4+UC
1.5%
98.5%
n=205
L. GLA+UC
8.3%
91.7%
n=200
Complexity value
▨ : 1.0–1.4
▨ : 1.4–1.6
■ : >1.8

Figure 5. Negatively stained PR8 virions. Representative electron micrographs of (A) unfixed virions (Unfixed), (B) OsO_4-fixed virions (OsO_4), (C) GLA-fixed virions (GLA), (D) unfixed and ultracentrifuged virions (Unfixed+UC), (E) OsO_4-fixed and ultracentrifuged virions (OsO_4+UC), and (F) GLA-fixed and ultracentrifuged virions (GLA+UC). Proportion of shape complexity values for the (G) Unfixed sample, (H) OsO_4 sample, (I) GLA sample, (J) Unfixed+UC sample, (K) OsO_4+UC and (L) GLA +UC sample is shown. Respective shape complexity values are given above the photos. The total number of analyzed virions is shown beneath the circles. Scale bar, 100 nm.

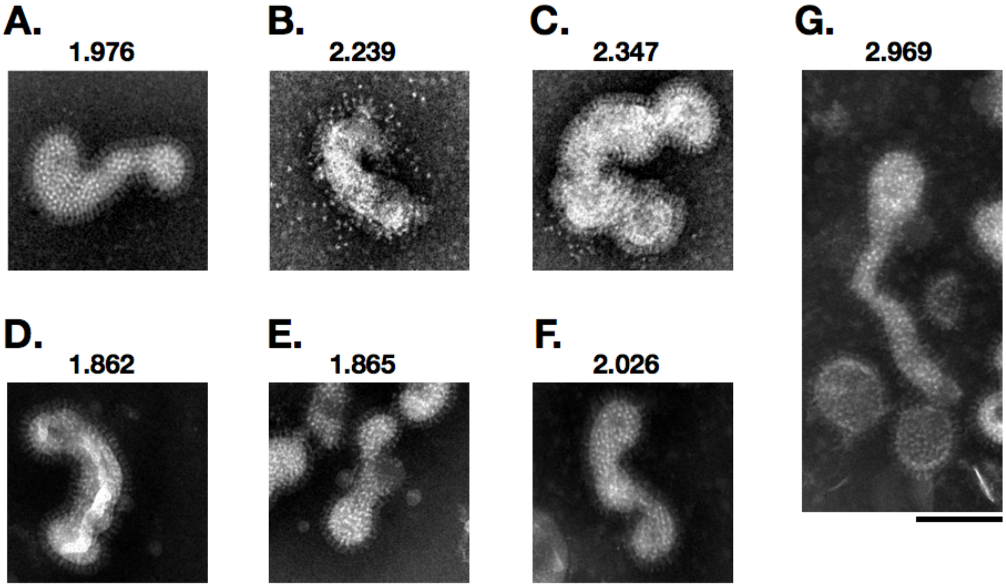

Figure 6. Irregular-shaped PR8 virions with complexity values >1.8. Examples of extremely irregular virions categorized into the complexity value >1.8 group. (A–C) unfixed and non-ultracentrifuged virions. (D–G) unfixed and ultracentrifuged virions. Respective shape complexity values are given above the photos. Scale bar; 100 nm.

virions were slightly altered into a round shape after ultracentrifugation, most were homogenous and morphologically irregular virions were not observed (Fig. 5E and K). These results indicate that ultracentrifugation affects virion morphology and that the proportion of morphologically irregular virions increases after ultracentrifugation unless virions are first chemically fixed. Similarly, whereas non-ultracentrifuged Udorn virions commonly showed regularly tight cord-like structures, ultracentrifuged Udorn virions were irregularly crooked filamentous structures (Fig. 7)

Statistical analysis of the morphological changes caused by ultracentrifugation

To examine the morphological changes caused by ultracentrifugation quantitatively, the mean complexity values of each specimen were calculated by using the perimeters and areas of each virion, as described in the Methods (Table 1). There were no significant differences in the mean complexity values among unfixed, GLA-fixed, and OsO_4-fixed virions without ultracentrifugation (P>0.01) (Table 2), suggesting that negative staining itself does not cause significant morphological changes. Upon ultracentrifugation, the mean complexity value of unfixed virions significantly increased compared to that of

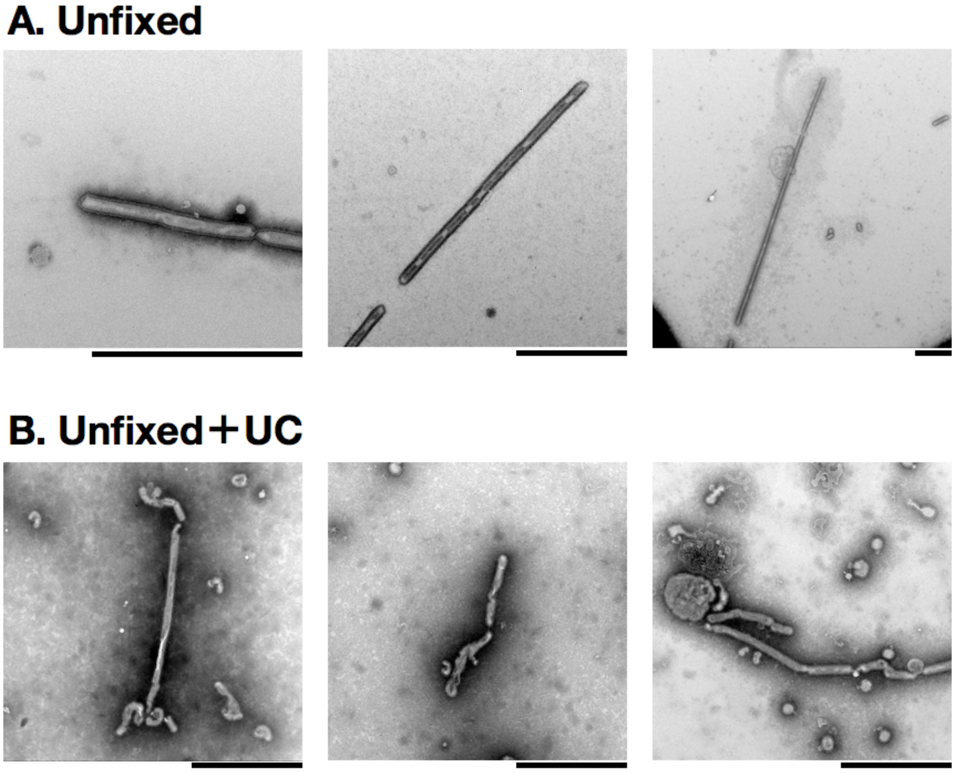

Figure 7. Negatively stained Udorn virions. Representative electron micrographs of (A) unfixed virions (Unfixed) and (B) unfixed and ultracentrifuged virions (Unfixed+UC). Scale bars, 1 µm.

Table 1. Mean complexity values

Sample	Mean complexity value*
Unfixed	1.233±0.162 (*n*＝218)
OsO_4	1.248±0.099 (*n*＝209)
GLA	1.229±0.112 (*n*＝215)
Unfixed＋UC	1.380±0.305 (*n*＝197)
OsO_4	1.196±0.104 (*n*＝205)
GLA＋UC	1.251±0.067 (*n*＝200)
Ultrathin-section TEM	1.268±0.071 (*n*＝216)
SEM	1.262±0.086 (*n*＝197)

*Mean complexity values (±SD) and the total number of PR8 virions analysed for each sample are shown.

Table 2. Comparison of mean complexity values

	P **value***
Unfixed vs OsO	0.266
Unfixed vs GLA	0.739
GLA vs OsO	0.062
Unfixed vs Unfixed＋UC	**4.779E-09**
OsO_4	**2.233E-08**
GLA vs GLA＋UC	0.022

*Comparison of the mean complexity values between the samples indicated. Statistical analyses were carried out using a non-parametric t-test. Statistically significant results (P<0.01) are shown in bold.

unfixed virions without ultracentrifugation (*P*<0.01) (Tables 1 and 2), indicating that the morphology of unfixed virions was significantly affected by ultracentrifugation. The mean complexity value of the OsO_4-fixed virions decreased significantly upon ultracentrifugation, indicating that these virions were more spherical compared to those without ultracentrifugation (*P*<0.01) (Fig. 5B, E and Tables 1 and 2). However, the mean complexity value of ultracentrifuged GLA-fixed virions was not statistically different from that of GLA-fixed virions without ultracentrifugation (*P*>0.01) (Table 2), suggesting that GLA fixation preserves virion morphology regardless of ultracentrifugation.

Morphology of an M2 tail deletion mutant as observed by using TEM

Previously, the role of the M2 cytoplasmic tail in viral morphology were examined, by demonstrating that an 11-amino acid deletion from the C-terminus of the M2 cytoplasmic tail does not affect virus growth, packaging efficiency of nucleoprotein (NP), or virion structure [5]. Here, to determine whether the M2 cytoplasmic tail is important for maintaining virion integrity, WSN wild-type and M2Δ11 viruses were generated by using reverse genetics [5, 20]. The viruses were propagated once in MDCK cells and purified by ultracentrifugation. Western blotting showed that the ratio of the viral structural proteins, HA, NP, M1 and M2, was comparable between the wild-type and the M2Δ11 viruses (Fig. 8A and B). Ultrathin-section TEM also demonstrated that there was no morphological difference between the two viruses and rod-like RNPs were observed in longitudinally sectioned virions as reported previously (Fig. 8C and D, left panels); the eight RNP segments were arranged in a specific pattern in cross-sectioned virions (Fig. 8C and D, right panels) [12].

Comparison of morphological changes in WSN wild-type and M2 tail deletion virions upon ultracentrifugation

To test the effect of the 11-amino acid deletion from the C-terminus of the M2 cytoplasmic tail on virion integrity, wild-type and M2Δ11 virions were examined by means of negative staining. The WSN virions were rounder than the PR8 virions as reported previously [11]. Without ultracentrifugation, both wild-type and M2Δ11 virions were uniformly spherical or elliptical, although a few irregular-shaped virions were

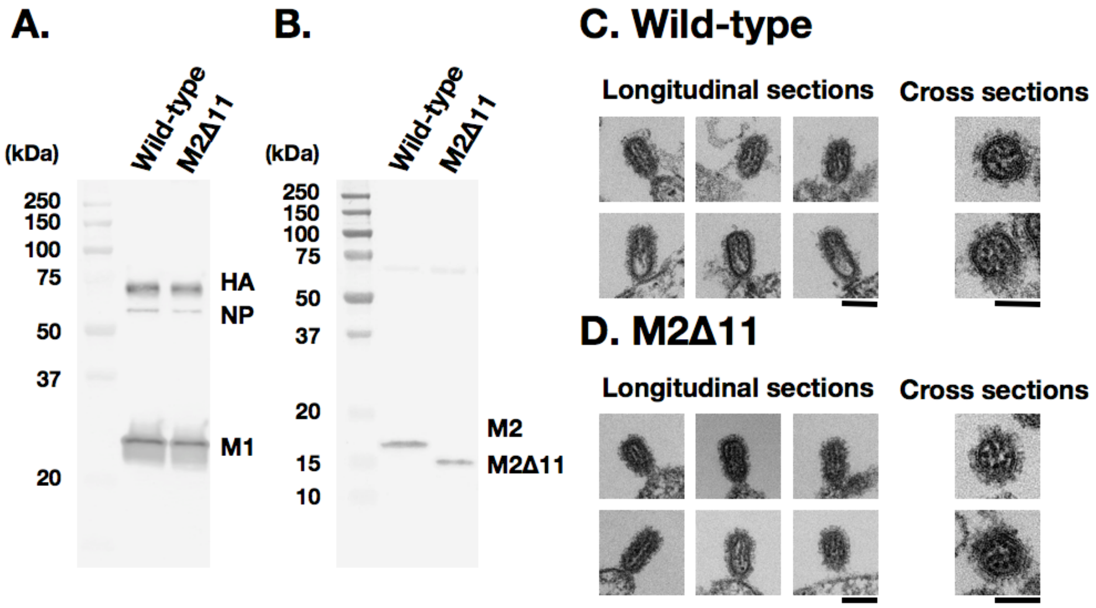

Figure 8. Comparison of WSN wild-type and M2Δ11 virions. (A and B) Western blot analysis of the structural proteins of the two viruses. (A) Viral proteins, HA, NP, and M1, were separated by using SDS-PAGE under nonreducing conditions and detected with an anti-influenza virus rabbit polyclonal antibody (R309) (B) Under reducing conditions, monomeric M2 proteins were detected with an anti-M2 (14C2) monoclonal antibody. (C and D) WSN wild-type and M2Δ11 virions observed by use of ultrathin-section TEM. Rod-like RNPs can be seen in all of the virions. Scale bars, 100 nm.

observed (Fig. 9A and B). Proportion of shape complexity values were similar between wild-type and M2Δ11 viruses without ultracentrifugation, and 1.0% or 0.5% of the wild-type and M2Δ11 virions, respectively, fell into the 1.4–1.8 group (Fig. 9E and F). Mean complexity values of the wild-type and M2Δ11 virions were similar and there was no significant difference between the two viruses ($P>0.01$) (Tables 3 and 4). As was the case with PR8 virions, both the unfixed WSN wild-type and the M2Δ11 virions changed their morphology after ultracentrifugation (Fig. 9C and D). Importantly, the structures of the M2Δ11 virions were substantially deformed after ultracentrifugation and most virions had irregular shapes (Fig. 9D). A total of 31.4% of them fell into the 1.4–1.8 group and 1.7% were in the >1.8 group, whereas 8.0% of the wild-type virions were in 1.4–1.8 group (Fig. 9G and H). Upon ultracentrifugation, the mean complexity values of both the wild-type and the M2Δ11 virions were significantly increased (Table 4). Moreover, the mean complexity value of the ultracentrifuged M2Δ11 virions was significantly greater than that of the wild-type virions (Table 4), indicating that the morphological changes in the M2Δ11 virions upon ultracentrifugation were much

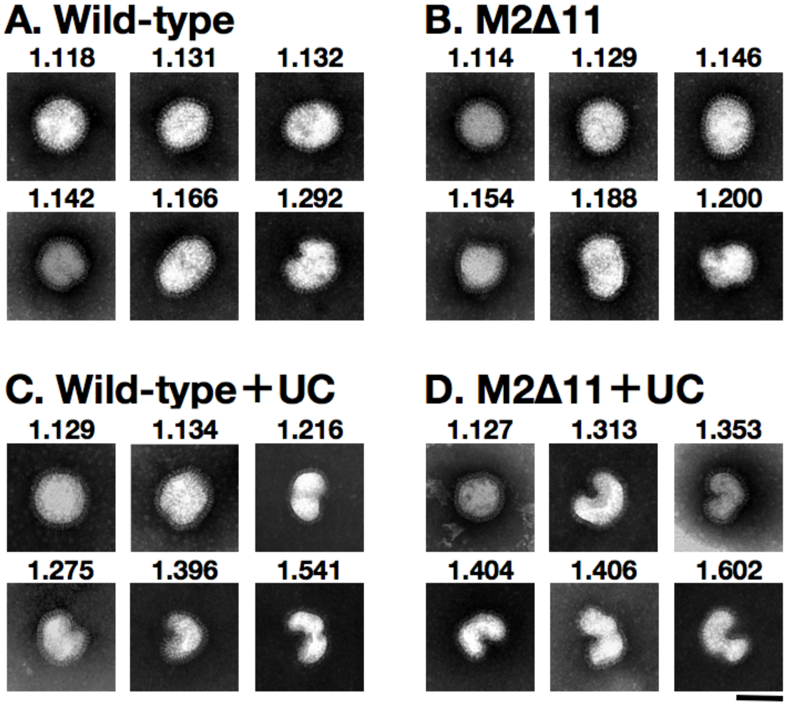

Figure 9. Negatively stained WSN virions. Representative electron micrographs of (A) WSN wild-type virions, (B) M2Δ11 virions, (C) ultracentrifuged wild-type virions (Wild-type+UC), and (D) ultracentrifuged M2Δ11 virions (M2Δ11+UC). Proportion of shape complexity values for the (E) Wild-type sample, (F) M2Δ11 sample, (G) Wild-type+UC sample, and (H) M2Δ11+UC sample are shown. Respective shape complexity values are given above the panes. The total number of analyzed virions is shown beneath the circles. Scale bar, 100 nm.

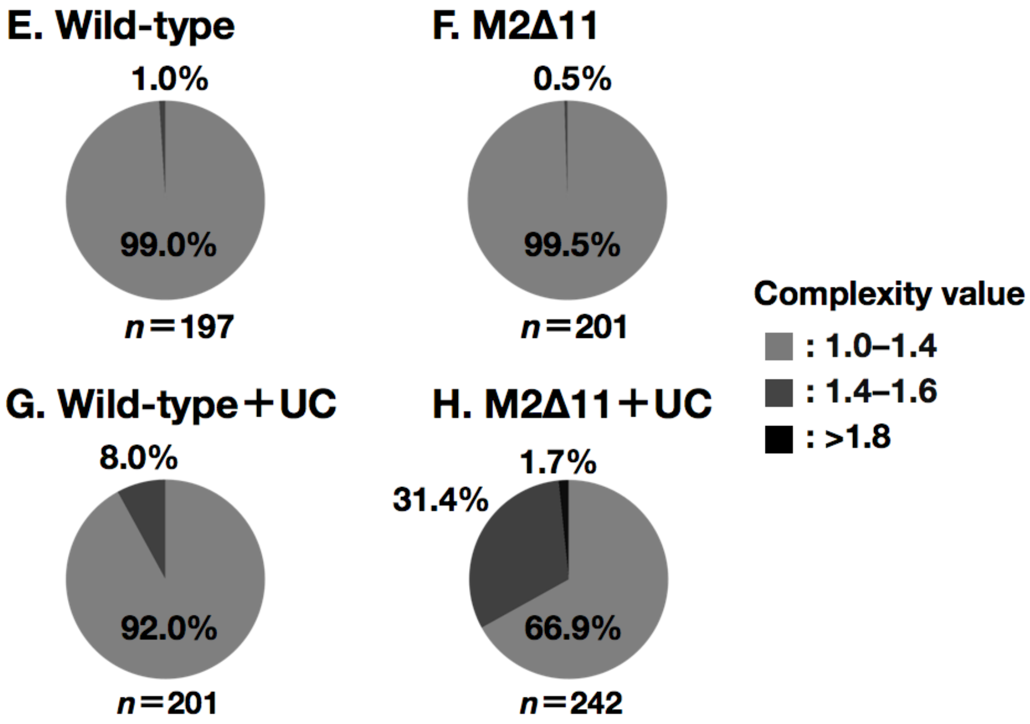
E. Wild-type
1.0%
99.0%
n=197
F. M2Δ11
0.5%
99.5%
n=201
G. Wild-type+UC
8.0%
92.0%
n=201
H. M2Δ11+UC
1.7%
31.4%
66.9%
n=242
Complexity value
: 1.0–1.4
: 1.4–1.6
: >1.8

Table 3. Mean complexity values

Sample	Mean complexity value*
Wild-type	1.167±0.076 (*n*＝197)
M2Δ11	1.159±0.060 (*n*＝201)
Wild-type＋UC	1.217±0.106 (*n*＝201)
M2Δ11＋UC	1.353±0.165 (*n*＝242)

*Mean complexity values (±SD) and the total number of the virions analysed for each sample are shown.

Table 4. Comparison of mean complexity values

	P* value
Wild-type vs M2Δ11	0.199
Wild-type vs Wild-type＋UC	**8.2E-08**
M2Δ11 vs M2Δ11＋UC	**2.77E-46**
Wild-type＋UC vs M2Δ11＋UC	**8.887E-23**

*Comparison of the mean complexity values between the samples indicated. Statistical analyses were carried out using a non-parametric t-test. Statistically significant results (*P*<0.01) are shown in bold.

greater than those in wild-type virions.

I.5 DISCUSSION

It is widely accepted that typical influenza A virions are spherical, elliptical, or filamentous, but that sometimes irregular-shaped virions are observed following negative staining. Such morphological features reflect the pleomorphism of influenza virions [15, 24]. Here, I found that virion morphology is significantly affected by ultracentrifugation, which is often involved in the negative staining process, resulting in the generation of morphologically irregular virions. However, the morphology of virions fixed with GLA was relatively conserved even after ultracentrifugation.

When virions fixed with GLA, a reagent that cross-links adjacent proteins [25], were ultracentrifuged, they maintained their uniformly spherical or oval shapes. In these virions, membrane-bound M1 molecules, which form a layer underneath the lipid envelope [26, 27], were tightly cross-linked to each other by GLA, presumably ensuring that the virion shape was conserved (Fig. 5F and L). On the other hand, when virions fixed with OsO_4 were ultracentrifuged, the virions tended to change to round rather than irregular structures (Fig. 5E and K). This morphological change likely reflects the fact that OsO_4 fixes mainly lipid membranes rather than proteins [25], which is insufficient to maintain the protein-protein interactions of the transmembrane proteins and M1 when faced with the physical impact of ultracentrifugation, although the lipid fixation protects the viral envelope from complete deformation into an irregular shape. For ultrathin-section TEM and SEM of budding virions, sample processing begins with GLA and OsO_4 chemical fixation, and does not involve ultracentrifugation. Therefore, the virion structures are relatively conserved during sample processing, and irregular virions were not found on ultrathin-section TEM and SEM analyses (Fig. 3 and 4). Taken together, I suggest that ultracentrifugation is a major cause of morphological artifacts with unfixed influenza virions and that the native structure of influenza virions is uniformly spherical, elliptical, or filamentous.

A recent study showed that the M2 cytoplasmic tail directly interacts with M1 through residues 71–76 in M2 and plays an essential role in viral assembly [28]. Because the mutant virus tested in this study still possessed the ability to bind to M1, the deletion did not affect virion morphology or the incorporation of M1 or the other viral proteins into virions (Fig. 8). Nevertheless, the integrity of the mutant virions upon ultracentrifugation was considerably decreased (Fig. 9 and Table 4), suggesting that the C-terminal 11 amino acids of M2 are involved in interactions with viral components (e.g., M1). The fragility of the M2 tail mutant may explain its suboptimal growth compared to that of wild-type virus [5].

Concentration and purification of specimens by ultracentrifugation facilitate structural analyses when using cryoelectron microscopy (cryoEM) or negative-staining electron microscopy. However, their artifactual effects, especially on fragile and fusion-capable lipid-vesicle samples such as enveloped virions, must be considered. Although cryoEM, which is used to observe native structures of unfixed, unstained, and frozen hydrated specimens, has been used to document morphologically irregular influenza virions in purified samples [11, 29-31], such virions are unlikely to reflect the native structure of those virions due to sample processing involving ultracentrifugation. The artifactual effects caused by using ultracentrifugation should be fully considered when undertaking detailed morphological analyses of enveloped viruses, including influenza viruses.

Chapter II

Orientations of the Influenza Viral Ribonucleoprotein Complexes

II.1 ABSTRACT

The influenza A virus possesses an eight-segmented, negative-sense, single-stranded RNA genome (vRNA). Each vRNA segment binds to multiple copies of viral nucleoproteins and a small number of heterotrimeric polymerase complexes to form a rod-like RNP, which is essential for the transcription and replication of the vRNAs. However, how the RNPs are organized within the progeny virion is not fully understood. Here, by focusing on polymerase complexes, I analyzed the fine structure of purified RNPs and their orientations within virions by using various EM. I confirmed that the individual RNPs possess a single polymerase complex at one end of the rod-like structure and that, by using immune electron microscopy, some RNPs are incorporated into budding virions with their polymerase-binding ends at the budding tip, whereas others align with their polymerase-binding ends at the bottom of the virion. These data further our understanding of influenza virion morphogenesis.

II.2 INTRODUCTION

Influenza A virus is a member of the family *Orthomyxoviridae*, with an eight-segmented and single-stranded genomic RNA (vRNA) of negative polarity. The vRNA is associated with multiple copies of nucleoproteins (NPs) and a small number of heterotrimeric RNA-dependent RNA polymerase complexes that comprise PA, PB1, and PB2, which together form the RNP. The RNP functions as a minimal unit responsible for the transcription and replication of the vRNA.

RNPs have twisted rod-like structures of approximately 13 nm in diameter; a string of NP beads folds back on itself, forming a loop structure at one end [32]. These rod-like structures range in length from 30 to 110 nm, which is consistent with the lengths of the respective vRNA segments [33]. The conserved and partially complementary sequences of the 5′ and 3′ ends of the vRNA form a promoter region, with which the viral polymerase complex is thought to associate [34-38]. Immuno-electron microscopy (Immuno-EM) of purified RNPs suggested that only one or a few polymerase complexes are located at the end of the rod-like RNP [39, 40], and that, therefore, the polymerase complexes are located at the opposite end to the RNP loop. In addition, recent single particle analyses revealed the three-dimensional (3D) structure of native RNPs, in which the polymerase complex was located at the end [41, 42]. However, the polymerase complex has still not been directly visualized without averaging techniques, because the 3D structure generated by single particle analysis is the average image from many different RNPs; it cannot provide information about the structure of individual RNPs.

Recent studies have shown that the eight unique vRNA segments that form RNPs are selectively packaged into each virion through segment-specific packaging signals that are present at the 5′ and 3′ ends of the vRNA segments [12, 43-46]. It has also been demonstrated by EM that the eight RNPs within the virions are arranged in a characteristic pattern – seven RNPs surround a central RNP – and that this set of eight RNPs associate vertically with an inner viral envelope at the tip of the budding virion [12, 44]. On the basis of these recent findings, the eight RNPs are thought to be coordinately arranged and incorporated into progeny virions. However, the orientations of the eight RNPs within budding virions are still not fully understood.

Here, I sought to determine the orientations of RNPs within the budding virion in more detail to better understand virion morphogenesis. To this end, I first conducted scanning transmission electron microscopy (STEM) tomography to clarify the number and exact location of the polymerase complexes in individual RNPs without using averaging techniques. Then, based on the information obtained from the STEM tomography, I analyzed the orientations of the RNPs within the budding virion by using immuno-EM.

II.3 MATERIALS AND METHODS

Antibodies

Mouse anti-NP (2S347/3), anti-PA (65/4), anti-PB1 (8/9), anti-PB2 (18/1), and anti-DYKDDDDK tag (anti-FLAG; Wako Pure Chemical Industries) monoclonal antibodies were used for immuno-EM. Goat anti-mouse IgG antibody conjugated to 10-nm gold particles was purchased from BBInternational.

Virus preparation

A stock of PR8 strain was prepared in chicken embryos as described in Materials and Methods in Chapter I. The virions were ultracentrifuged through a sucrose gradient and purified.

RNP purification

Purified PR8 virions were lysed in a solution containing 50 mM Tris-HCl (pH＝8.0), 100 mM KCl, 5 mM $MgCl_2$, 1 mM DTT, 2% lysolecithin, 2% Triton X-100, 5% glycerol, and 1U/µl RNase inhibitor (Promega) for 1 h at 30 ºC. The sample was then directly ultracentrifuged through a 30%–70% glycerol gradient at 245,000 x *g* for 3 h at 4 ºC.

Gel electrophoresis and staining

After ultracentrifugation through 30%–70% glycerol gradients, the fractions were mixed with 2× Tris/glycine SDS sample buffer (Invitrogen) and subjected to SDS-PAGE, followed by Coomassie brilliant blue staining (CBB Stain One; Nacalai Tesque).

Negative-staining immuno-EM

Purified RNPs were adsorbed to formvar-coated nickel grids and pre-fixed with 1% glutaraldehyde (GLA). The grids were washed, treated with blocking solution (Blocking One; Nacalai Tesque), and then incubated with an anti-NP, anti-PA, anti-PB1, anti-PB2 antibody, or anti-FLAG antibody conjugated with 5-nm gold particles (BBInternational). After being washed, the samples were fixed with 1% GLA and negatively stained with 1% UA. The images were recorded with a Tecnai F20 TEM (FEI Company) operated at 200 kV.

STEM tomography and image analysis

Purified RNPs were adsorbed onto carbon-coated copper grids, negatively stained with 1% UA, and then air dried. The single- or dual-axis tomographic images of the negatively stained RNPs were obtained on a high-angle annular dark-field detector (Fischione) with a field emission STEM operated at 200 kV (Tecnai F20; FEI Company). The x- and y-axis tilted series of the RNP images were collected by 2cosθ° each up to ± 60° (75 images) at 0.18 to 0.26 nm per pixel. The raw images were reconstructed into a 3D volume by using Inspect3D software (FEI Company). For dual-axis STEM tomography, two volumes obtained from the x- and y-axis tilted series were combined by using Inspect3D software. Digital slices (0.18- to 0.26-nm thick) were visualized with the Avizo 6.2 image processing package (Visualization Science Group).

Ultrathin-section immuno-EM

The chemically fixed sample of PR8-infected allantoic membranes was prepared as described in Materials and Methods in Chapter I. Sections of the sample (80-nm thick) were etched on nickel grids with saturated sodium periodate solution, washed with 0.2

M glycine in PBS, and treated with the blocking solution. The grids were then incubated with an anti-NP, anti-PB2, anti-PB1, anti-PA, or anti-FLAG monoclonal antibody. After being washed with PBS, they were incubated with a goat anti-mouse immunoglobulin conjugated to 10-nm gold particles. The samples were washed, fixed with 1% GLA, and stained with 2% UA and Reynolds' lead. The digital images were recorded with TEM operated at 200 kV.

Distribution analysis of the NP and polymerases within the virions

Longitudinally sectioned virions containing rod-like RNPs were randomly selected in the images from the ultrathin-section immuno-EM. The distribution of gold signals in the virions was examined by measuring the distances from the budding tip of the virions to the gold signal by using ImageJ software.

Theoretical models for molecular distribution patterns on RNPs

I constructed four theoretical distribution models in which the molecules are evenly distributed on the eight RNPs (NP Model), located at the ends of the RNPs only at the budding tip (Polymerase Model 1), located at the bottom end (Polymerase Model 2), or located at both ends (Polymerase Model 3). The lengths of the RNPs were assumed to be proportional to the number of nucleotides in the respective vRNA segments (100, 100, 95, 76, 67, 60, 44, and 38 nm for segment #1 to #8, respectively). For the NP Model, each molecule was considered to be located at intervals of 2.0 nm on the RNPs, on the basis of previous reports showing that each NP molecule binds to 24 nucleotides of viral RNA [41]. The gold signals that reacted to each molecule were considered to be normally distributed. The data analysis and graph creation were done by using R packaging version 2.15.1 [47].

II.4 RESULTS

STEM tomography of purified RNPs

The polymerase complex is located at the end of the RNP, whose 3D structure was recently visualized by use of single particle analysis [41, 42]. This analysis, however, provides structural information by averaging many different molecules. Therefore, the polymerase complex has still not been directly visualized without averaging techniques. To determine the exact location and the number of polymerase complexes on individual RNPs, I extracted RNPs from purified virions. Gel electrophoresis and negative-staining EM of the purified RNPs showed that the specimen was highly purified with few disrupted RNPs or debris from the other viral components (Fig. 10). I then conducted negative-staining immuno-EM with monoclonal antibodies against the respective RNP components. I found that the polymerase subunits were exclusively detected at one end of the rod-like RNP, whereas NP molecules were detected along the entire length of the rod-like structure of the RNP (Fig. 11). These results are in good agreement with a previous study [39, 40]. Next, I attempted to visualize the polymerase complex binding

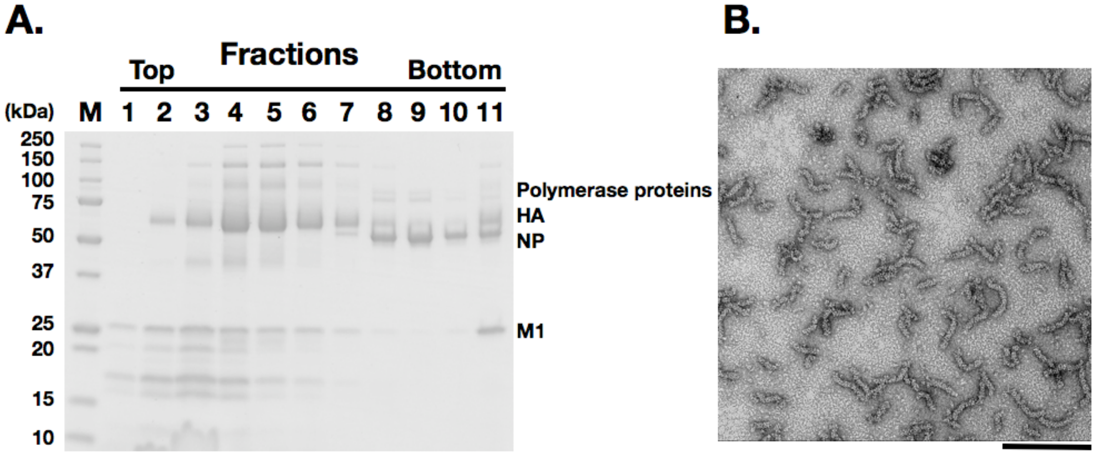

Figure 10. Isolation and purification of RNPs. (A) Gel electrophoresis of the proteins of each fraction after ultracentrifugation through 30%–70% glycerol gradients. Fractions 8 and 9, containing NP and polymerase proteins, were used for the RNP observations. (B) A representative electron micrograph of the RNPs at a low magnification. M; Molecular marker. Scale bar, 200 nm.

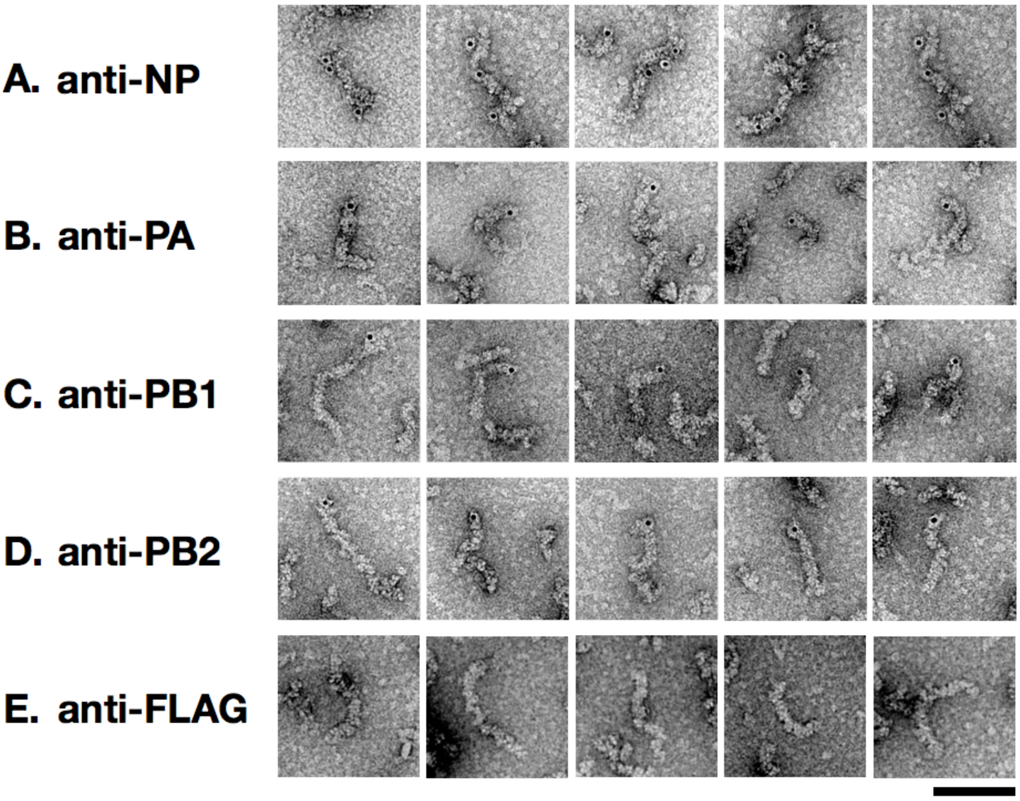

Figure 11. Negative-staining immuno-EM of purified RNPs with an (A) anti-NP, (B) anti-PA, (C) anti-PB1, (D) anti-PB2 antibody, or (E) anti-FLAG antibody conjugated with 5-nm gold particles. I analyzed 21 RNPs labeled with an anti-PA antibody, 16 RNPs with an anti-PB1 antibody, 23 RNPs with an anti-PB2 antibody, and 35 RNPs with an anti-NP antibody. All of the RNPs labeled with anti-polymerase antibodies had only a single gold bead, whereas those labeled with the anti-NP antibody had one to four gold beads which were distributed throughout the RNP. Scale bar, 50 nm.

to the end of the RNP by using STEM tomography. Electron tomography is a technique used to construct detailed 3D structures of macromolecules; STEM tomography provides a better contrast and signal-to-noise ratio than does conventional electron tomography, producing high resolution images [48, 49]. Upon reconstruction of images by using STEM tomography, I was able to visualize the constituent molecules of the RNP (Fig. 12A). At one end of the RNP, a loop structure was formed by several molecules that were uniform in shape and about 4 by 6 nm (Fig. 12, arrowheads); this is consistent with a previous report of NP molecules of 3.5 by 6.2 nm forming a small rod-like structure [50]. In 50 out of the 323 RNPs (15.5%), I observed a single molecule of about 10 nm in diameter only at the blunt end opposite the loop structure. The morphology of this molecule, which sometimes showed a holey or grooved structure (Fig. 12A, arrows in the left panels), is consistent with the polymerase complex visualized by single particle analyses [41, 42, 51, 52]. Serial slices of the RNPs showed that the molecule has a different electron density from NP molecules (Fig. 12A, arrows in the right small panels), suggesting that the molecule observed at the end of the RNP

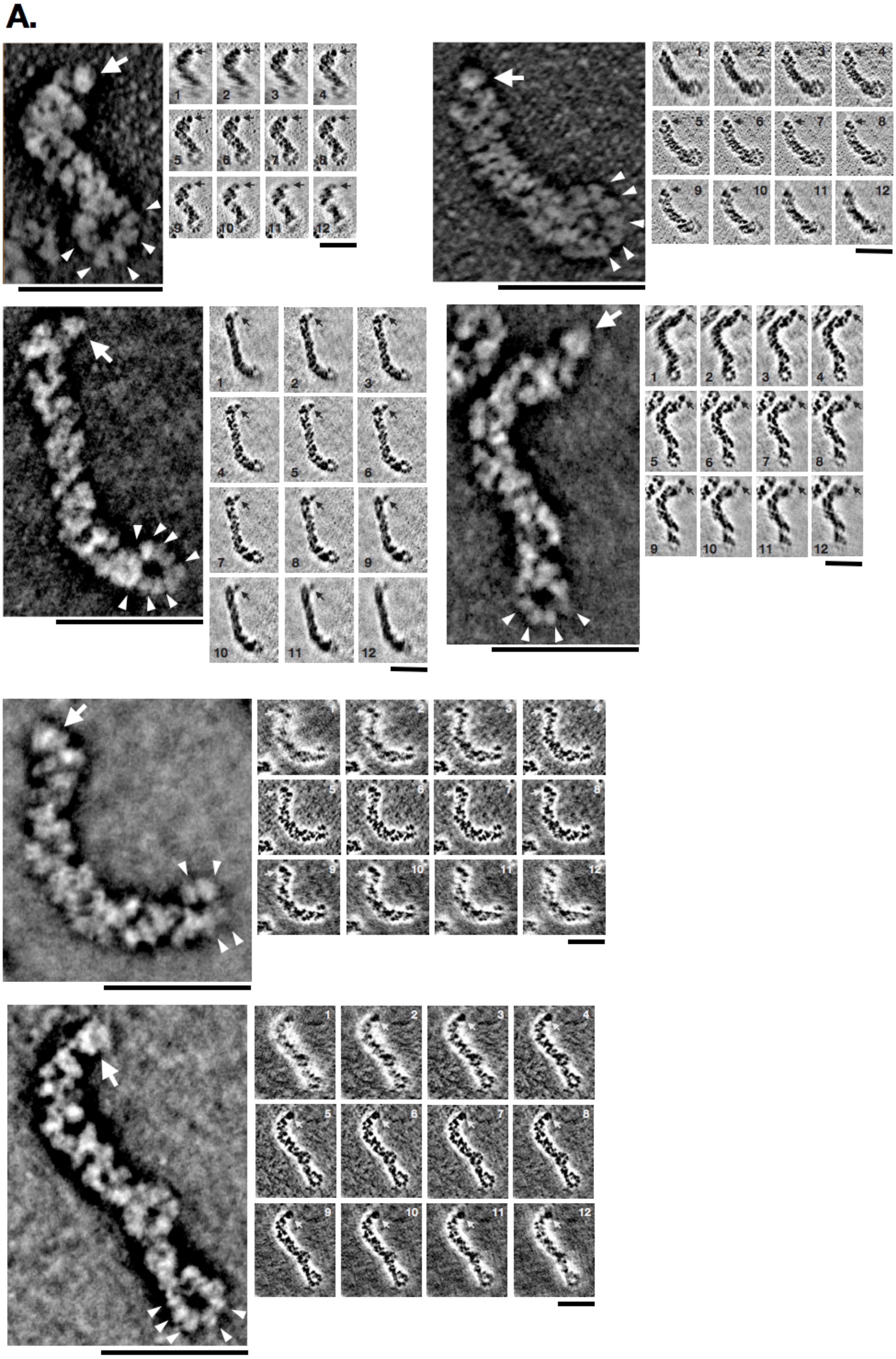
A.
1
2
3
4
5
6
7
8
9
10
11
12

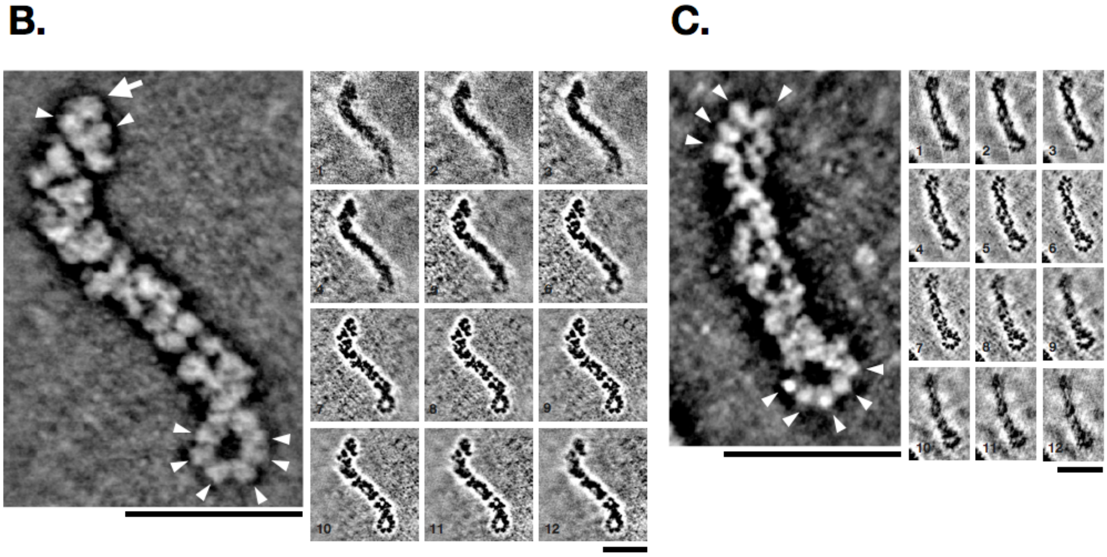

Figure 12. Reconstructed 0.18- to 0.26-nm-thick digital slice views of purified RNPs by STEM tomography. Large panels on the left show representative contrast-turned slice views of the RNPs; small panels on the right show serial sections of RNPs at 0.18- to 0.26-nm intervals. (A) At one end of the RNP, NP molecules form a loop structure (arrowheads). A molecule with a holey or grooved structure (arrow on the left panels) of about 10 nm in diameter, which is morphologically different from NP molecules, is visible at the opposite end of the loop structure. (B) An RNP containing a molecule that is not clearly distinguishable from NP (arrow on the left panel). (C) An RNP that probably does not contain a polymerase. Scale bars, 50 nm.

is most likely a single polymerase complex. I never observed two or more polymerase complexes on the RNPs. Taken together, my observations strongly suggest that only a single polymerase complex is present at the opposite end of the loop structure of a rod-like RNP.

Immuno-EM of thin-sectioned virions

Within a budding virion, eight RNPs are associated vertically with the envelope at the tip [12, 44]. However, it remains unclear whether the polymerase-binding ends of the eight RNPs are present at the tip or at the middle or bottom portions of the budding virion. To clarify this point and determine the orientations of the eight RNPs within the budding virion in more detail, I analyzed the location of the polymerase subunits, which bind to the blunt end of the rod-like RNP (Fig. 12), within budding virions by using immuno-EM. After immuno-gold labeling with the respective monoclonal antibodies, I randomly chose longitudinally sectioned budding virions, in which the whole rod-like RNP complexes were visible (Fig. 13A–G). I saw no significant signal when immuno-EM was conducted with an anti-FLAG antibody or without a primary antibody (Fig.

13E and F). Then, the distances between the immuno-gold signal and the budding tip of the virions were measured (Fig. 13H). I found that the NP signals were distributed along the length of the rod-like RNPs in the virions with a broad peak at 30 to 90 nm from the virion budding tip (Fig. 13I, left); there were also a few signals with anti-FLAG. The reduction in NP signals at around 100 to 150 nm from the tip of the virion is consistent with reports that the eight RNPs within the virion are associated with the tip of the budding virion and are different in length [12, 44]. On the other hand, the signals of the various polymerase subunits were distributed with a peak of around 10 to 40 nm from the virion budding tip; however, a considerable number of the signals were also found at around 60 to 120 nm from the virion budding tip (Fig. 13I, the three graphs on the right). These results indicate that most of the polymerases are present underneath the budding tip of the virion, but some are also present in the middle and at the bottom portion of the virions. Importantly, in some virions, the polymerase signals were found at both the top and the middle or the top and the bottom portions of the budding virion (Fig. 13G) Thus, my results indicate that the some RNPs are incorporated with their

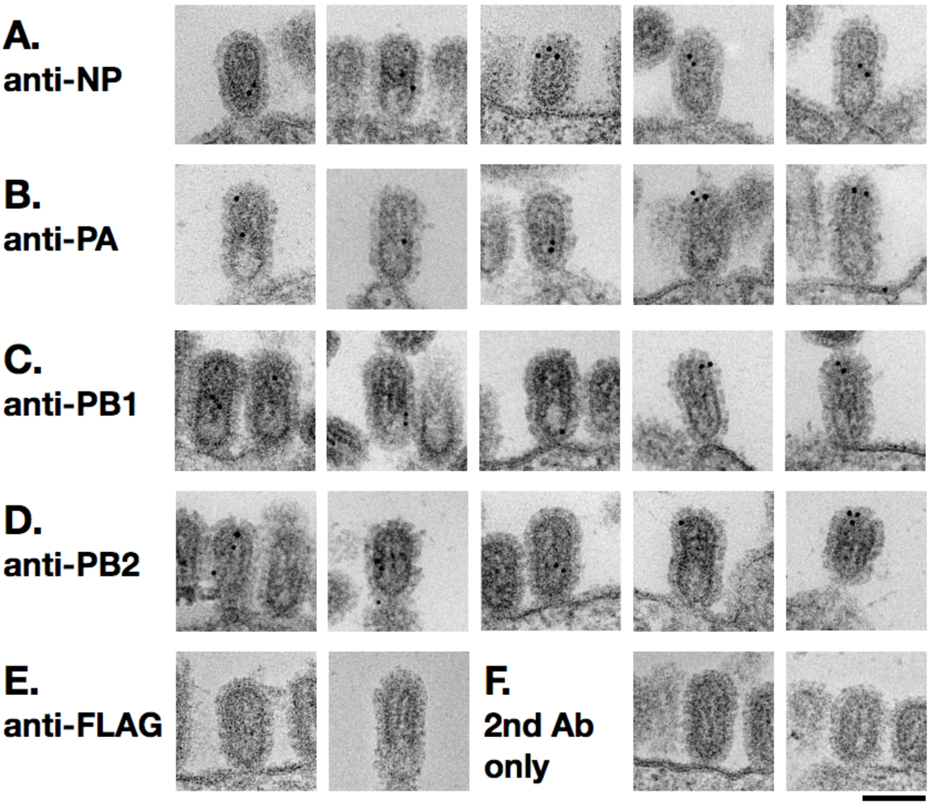

Figure 13. Immuno-staining of thin-sectioned virions. The sections were sequentially incubated with an (A) anti-NP, (B) anti-PA, (C) anti-PB1,(D) anti-PB2, or (E) anti-FLAG monoclonal antibody, or (F) without a primary antibody, and with a secondary antibody conjugated to 10-nm gold particles. The number of virions examined was: 211 for NP, 198 for PA, 178 for PB1, and 218 for PB2. (G) In some virions, the gold signals were simultaneously found both at the top and bottom of the same budding virion. (H) Distances between the budding tip of the virion and the gold-particle signals were measured. (I) Histograms indicating the distribution of NP, PA, PB1, and PB2 within the virions. Scale bars, 100 nm.

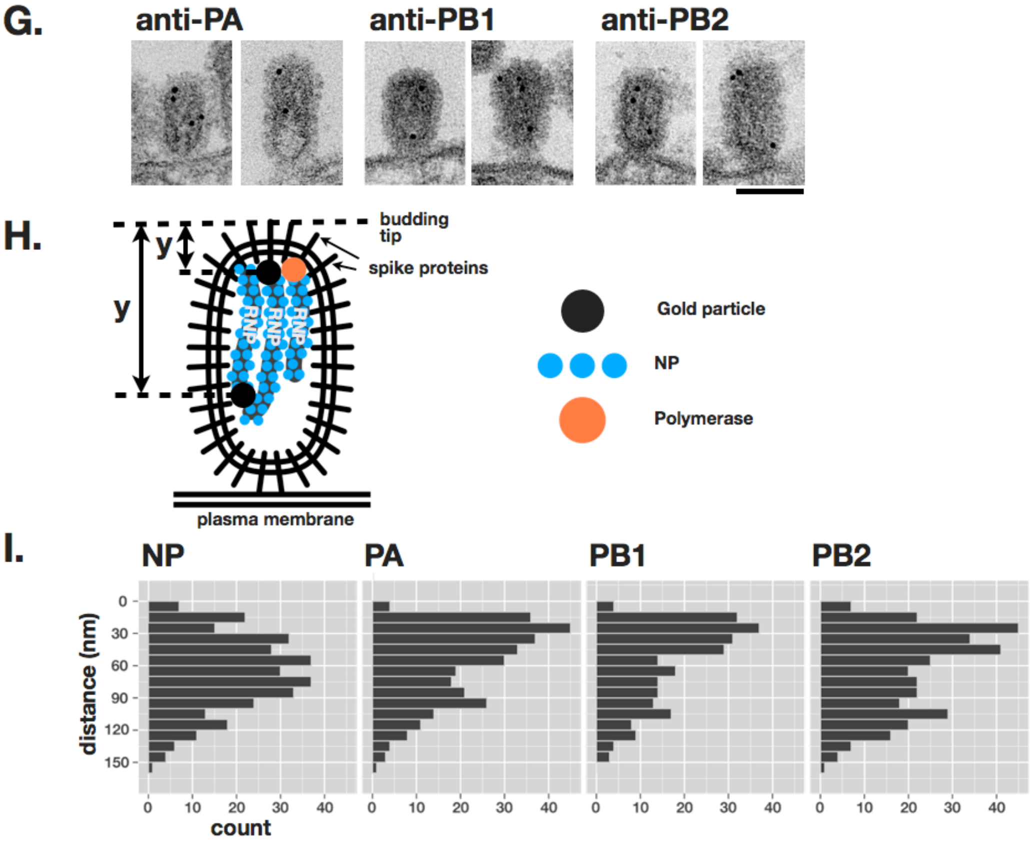
G.
anti-PA
anti-PB1
anti-PB2
H.
y
y
budding tip
spike proteins
RNP
RNP
RNP
plasma membrane
● Gold particle
●●● NP
● Polymerase
I.
NP
PA
PB1
PB2
distance (nm)
0
30
60
90
120
150
0
10
20
30
40
count

polymerase-binding ends toward the budding tip, whereas others are incorporated with their polymerase-binding ends toward the bottom of a virion (see Fig. 15B).

Distribution modeling of the NP and polymerase

To confirm my observations that polymerases are located at both the upper and lower portions of the virion, I constructed models for various distribution patterns on RNPs within the virion. The NP distribution Model showed a single peak at around the middle part of the virion, which agreed with the distribution of the anti-NP signals (Fig. 13I and 12C, left). Polymerase Model 1 showed a sharp peak at the budding tip of the virion. Because RNPs differ in length, the distribution of Polymerase Model 2 showed a broad peak(s) at the bottom part of the virion. The data obtained by immuno-EM of anti-polymerase antibodies was fitted to Polymerase Model 3, in which the molecules are located at the both tip and the bottom of the virion (Fig. 13I and 14C, right). This distribution model is characterized by a major sharp peak at the budding tip and a minor broad peak(s) at the middle/bottom of the virion. I analyzed the theoretical distributions by using three different standard deviations (10, 15 and 20 nm) of the normal

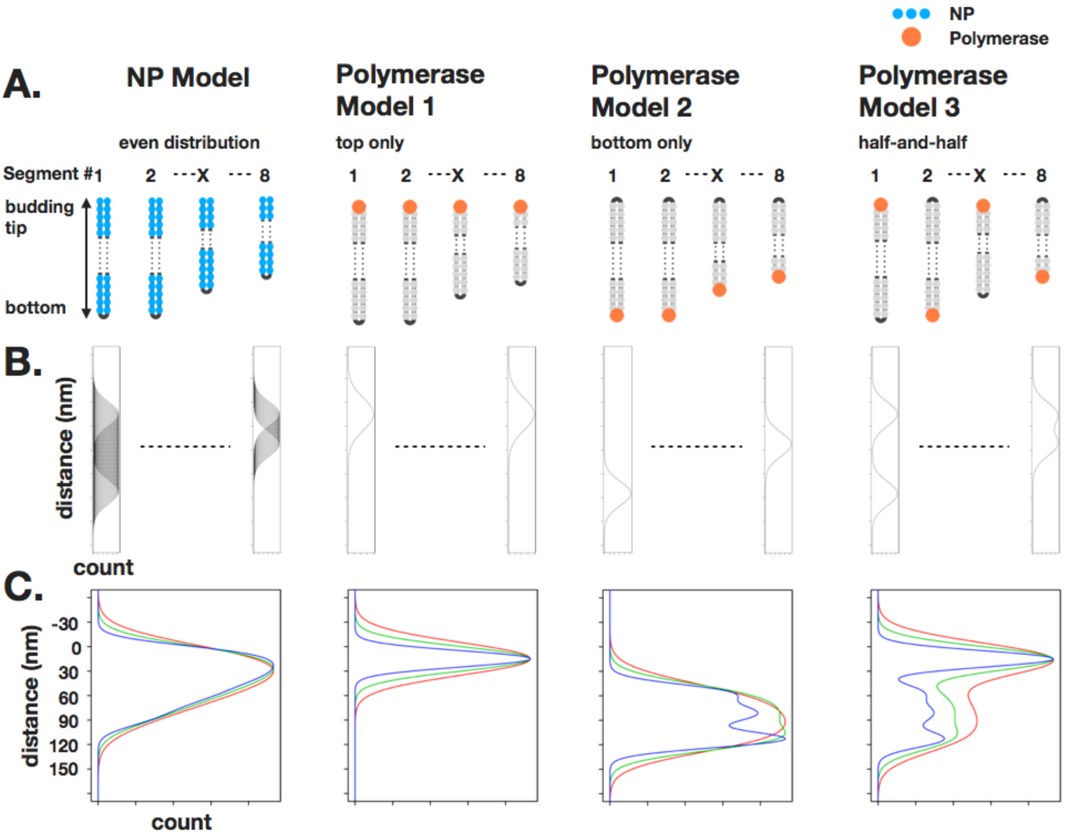

Figure 14. Molecular distribution models on RNPs. (A) Schematic diagrams of models showing even distribution on the RNPs (NP Model), localization only at the budding tip (Polymerase Model 1; top only), localization only at the bottom (Polymerase Model 2; bottom only), or localization at both positions (Polymerase Model 3; half-and-half). The blue and orange circles represent the NP and polymerase proteins, respectively. (B) Probability distribution curves for each vRNA segment for NP and Polymerase Models 1 to 3. The x-axis represents the number of signals; the y-axis represents the distance between the virion-budding tip and the gold signals. (C) Combined distribution curves for each model. For the respective models, three curves were constructed by using different standard deviations of 20 (red), 15 (green) or 10 nm (blue).

distributions for the distribution of each molecule, because the size of the primary and secondary antibody complex ranges from 10 to 20 nm (Fig. 14C). I found that the distribution pattern for Polymerase Model 3 was similar to the histograms obtained from immuno-EM by using anti-PA, PB1, or PB2 antibodies (Fig. 13I and 14C). Therefore, the slight differences in the distribution patterns of the PA, PB1, and PB2 signals likely stem from differences among the respective normal distributions of the conjugated antibodies.

II.5 DISCUSSION

It have not been fully understood how the eight RNPs within the influenza virus virion are arranged, even though such information is important to our understanding of virion morphogenesis. Here, by combining STEM tomography and immuno-EM, I have confirmed that a single polymerase complex is associated with a rod-like RNP at the blunt end of the budding virion and shown that the orientation of the polymerase-binding ends of the eight RNPs is not uniform within the budding virion.

A previous report estimated that there are more than nine polymerase complexes within an influenza virion [53]. However, the accuracy of this estimation remains unclear because my study as described in Chapter I showed that influenza virions could be fused during virion purification that involves ultracentrifugation [54]. In fact, immuno-EM and biochemical analyses indicate that a single polymerase complex is associated with one end of each of the eight RNP [35-42].

In this study, by using STEM tomography, I visualized the polymerase complex on a native RNP purified from virions (Fig. 12) without using averaging techniques such as single particle analysis [41, 42, 51, 52]. I confirmed that each RNP likely possesses only a polymerase complex at one end of the RNP, although polymerase complexes could not be clearly observed in some RNPs (Fig. 12B and C). This was likely because some polymerase complexes may have been too close to neighboring NPs to be distinguished by STEM tomography, or because they were inadvertently removed during the experimental manipulation. Since polymerase complexes can be dissociated during RNP purification that involves ultracentrifugation [35, 39, 40, 55], it remains unclear whether some RNPs lack the polymerase complex to begin with.

For decades, two conflicting genome packaging models have been considered: selective packaging and random packaging. Recent studies finally concluded that a set of eight vRNA segments (i.e., the eight RNPs) are selectively incorporated into every progeny virion [12, 43, 44, 46, 56]. Reverse genetics studies further demonstrated that all eight vRNA segments possess segment-specific packaging signal sequences at both the 5′ and 3′ ends of the vRNAs [57, 58]. It was also shown that mutations in the packaging signal of a vRNA segment affect the packaging efficiency of the other vRNA segments into virions [46, 59-61]. These findings imply that the eight RNPs within the virion interact with each other possibly via the packaging signals [45, 46], which are close to the polymerase-binding promoter region (Fig. 15A). If all eight of the RNPs have their polymerase-binding ends at the tip or the bottom of the budding virion, then interactions among the eight RNPs may be restricted at the tip or at the middle and bottom portions of that virion, respectively (Fig. 15C and D) [45, 46]. In the present study, however, the eight RNPs are differently oriented within virions (Fig. 15B). Therefore, interactions among RNPs do not appear to be restricted at a single side within the budding virion, which is consistent with the previous report that string-like intermediates exist between the RNPs throughout the virion [44]. On the other hand, there may be as-yet unidentified regions in the middle of the vRNA segments that are involved in efficient genome packaging. It remains unclear whether the orientation of the respective RNPs is the same within all budding virions. Further studies are needed to fully understand the selective packaging mechanism.

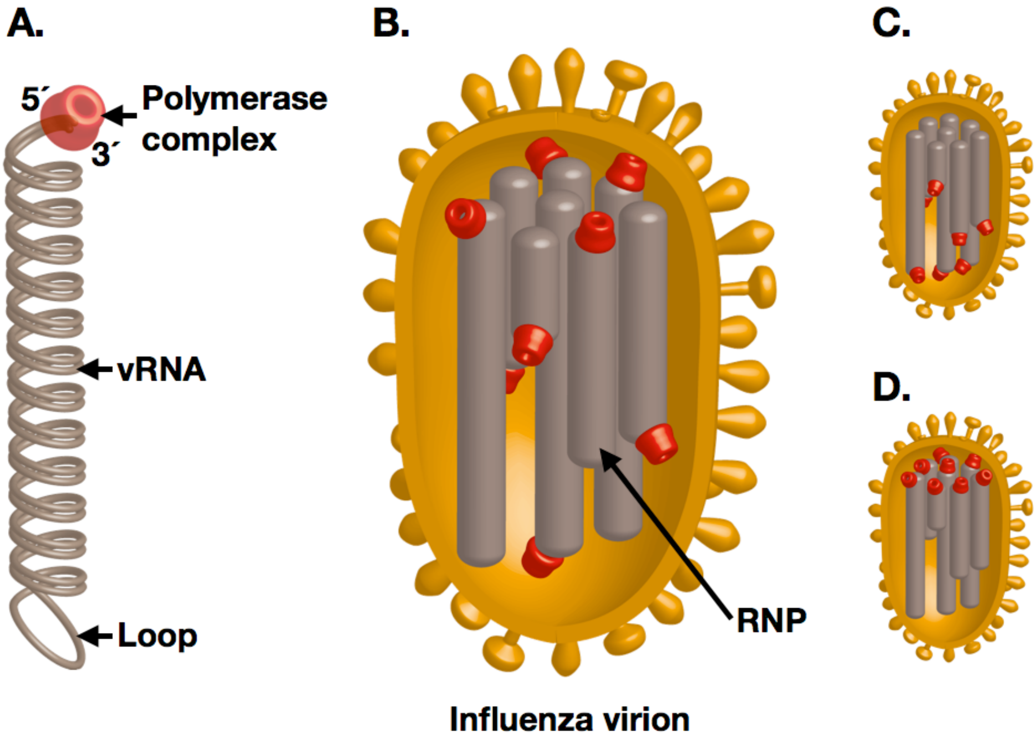

Figure 15. Schematic diagrams of RNPs within a virion. (A) The diagram showing a polymerase complex binding to the promoter region, which composed of the complementary sequences of the 5´ and 3´ ends of the vRNA [34, 35, 38, 55]. (B) A possible model, based on the results of this study, in which differently oriented RNPs are vertically packaged in a virion. (C and D) These models depict all eight RNPs as being aligned in the same direction within the virion, with the polymerase complex being at the bottom (C) or at the budding tip (D).

In conclusion, here I suggest that the eight RNPs are differently oriented within a virion. My study provides a novel model of the influenza virion structure and important insights for elucidating the mechanism of influenza virus genome packaging.

CONCLUDING REMARKS

Although the morphology of influenza A virus budding and purified virions has long been extensively studied by using various electron microscopies, we remain in the dark about the precise virion structure because of viral pleomorphism and genome segmentation, which complicate morphological and structural analyses and perplex researchers to the point where it becomes difficult to make a definite conclusion about virion morphogenesis. Here, I focused on several aspects of the morphogenesis of influenza A virus: its native morphology, structural integrity, and the interior structures of the virion.

Since the influenza virion was first visualized by using transmission electron microscopy in the early 1940s, it has been commonly believed that the irregular-shaped influenza virions are natural in shape [15, 24, 62, 63]. However, in Chapter I, I showed that these irregular-shaped virions were, in fact, artifacts caused mainly by ultracentrifugation during the virus purification process, and that the native morphology of the influenza virion is actually spherical, elliptical, or filamentous. I also showed in

Chapter I that the cytoplasmic tail of M2 is essential for virion integrity. This study showed not only the structural features of the influenza virion, but also the importance of sample preparation; experimental manipulations like ultracentrifugation, freeze-thawing, and air drying could easily cause artifacts when flexible and fusion-capable enveloped viruses are examined.

For decades, two contrary genome packaging models have been proposed: selective packaging and random packaging. Recent studies have concluded that a single set of eight-segmented RNAs representing the virus genome is selectively incorporated into the virion, and that the eight RNPs have a specific configuration, in which seven RNPs surround a central RNP within the virion [12, 43, 44]. However, the detailed configurations of the RNPs remain unclear. In Chapter II, I analyzed the orientations of the influenza viral RNPs within the virion by detecting the polymerase that is located only at the blunt end of each RNP. I found that the polymerase-binding ends of the RNPs are located both at the budding tip and at the bottom of the virion; the RNPs are differently oriented inside the virion, suggesting the presence of a complicated genome packaging mechanism.

In closing, my study on the interior and exterior architecture of the influenza virion have provided important clues to the mechanisms responsible for the formation of this infectious genome-carrying organism. Such findings may lead to the discovery of novel methods to inhibit virion formation and to the development of antiviral therapy to control influenza.

ACKNOWLEDGEMENTS

I would like to express my sincere gratitude to my supervisor, Professor Yoshihiro Kawaoka, for providing me with this precious opportunity to study as a Ph.D student in his laboratory. I especially would like to express my deepest appreciation to my supervisor, Dr. Takeshi Noda, for his careful guidance, considerable encouragement, and invaluable discussions that exercise my mind to improve my scientific thinking. I am very grateful to Dr. Hiroshi Sagara for his valuable mentorship regarding electron microscopy methodologies and his assistance with my experiments. I am also profoundly grateful to all members of Professor Kawaoka's Laboratory for excellent technical help and constant encouragement.

This work was supported by a Grant-in-Aid from the Japan Society for the Promotion of Science Fellows.

Finally, I would like to thank my friends and my family for their understanding, sincere encouragement, and continuing support throughout my studies.

REFERENCES

1. **Palese P, Shaw ML.** 2007. Orthomyxoviridae: the viruses and their replication, p. 1647-1689. *In* D. M. Knipe and P. M.Howley (ed.), Fields Virology, 5th, vol. 2. Lippincott Williams & Wilkins, Philadelphiafia.
2. **Bourmakina SV, Garcia-Sastre A.** 2003. Reverse genetics studies on the filamentous morphology of influenza A virus. Journal of General Virology **84:** 517-527.
3. **Elleman CJ, Barclay WS.** 2004. The M1 matrix protein controls the filamentous phenotype of influenza A virus. Virology **321:** 144-153.
4. **Roberts PC, Lamb RA, Compans RW.** 1998. The M1 and M2 proteins of influenza A virus are important determinants in filamentous particle formation. Virology **240:** 127-137.
5. **Iwatsuki-Horimoto K, Horimoto T, Noda T, Kiso M, Maeda J, Watanabe S, Muramoto Y, Fujii K, Kawaoka Y.** 2006. The cytoplasmic tail of the influenza A virus M2 protein plays a role in viral assembly. Journal of Virology **80:** 5233-5240.
6. **Jin H, Leser GP, Zhang J, Lamb RA.** 1997. Influenza virus hemagglutinin and neuraminidase cytoplasmic tails control particle shape. EMBO Journal **16:** 1236-1247.
7. **Bachi T, Gerhard W, Lindenmann J, Muhlethaler K.** 1969. Morphogenesis of influenza A virus in Ehrlich ascites tumor cells as revealed by thin-sectioning and freeze-etching. Journal of Virology **4:** 769-776.

8. **Compans RW, Dimmock NJ.** 1969. An electron microscopic study of single-cycle infection of chick embryo fibroblasts by influenza virus. Virology **39:** 499-515.

9. **Morgan C, Rose HM, Moore DH.** 1956. Structure and development of viruses observed in the electron microscope. III. Influenza virus. Journal of Experimental Medicine **104:** 171-182.

10. **Morgan C, Hsu KC, Rifkind RA, Knox AW, Rose HM.** 1961. The Application of Ferritin-Conjugated Antibody to Electron Microscopic Studies of Influenza Virus in Infected Cells : I. The Cellular Surface. Journal of Experimental Medicine **114:** 825-832.

11. **Nayak DP, Balogun RA, Yamada H, Zhou ZH, Barman S.** 2009. Influenza virus morphogenesis and budding. Virus Research **143:** 147-161.

12. **Noda T, Sagara H, Yen A, Takada A, Kida H, Cheng RH, Kawaoka Y.** 2006. Architecture of ribonucleoprotein complexes in influenza A virus particles. Nature **439:** 490-492.

13. **Almeida JD, Waterson AP.** 1967. A morphological comparison of Bittner and influenza viruses. Journal of Hygiene **65:** 467-474.

14. **Ruigrok RW, Wrigley NG, Calder LJ, Cusack S, Wharton SA, Brown EB, Skehel JJ.** 1986. Electron microscopy of the low pH structure of influenza virus haemagglutinin. EMBO Journal **5:** 41-49.

15. **Stevenson JP, Biddle F.** 1966. Pleomorphism of influenza virus particles under the electron microscope. Nature **212:** 619-621.

16. **Wrigley NG.** 1979. Electron microscopy of influenza virus. British Medical Bulletin **35:** 35-38.

17. **Almeida JD, Waterson AP.** 1967. Some observations on the envelope of an influenza virus. Journal of General Microbiology **46:** 107-110.

18. **Nermut MV, Frank H.** 1971. Fine structure of influenza A2 (Singapore) as revealed by negative staining, freeze-drying and freeze-etching. Journal of General Virology **10:** 37-51.

19. **Ruigrok RW, Hewat EA, Wade RH.** 1992. Low pH deforms the influenza virus envelope. Journal of General Virology **73:** 995-998.

20. **Neumann G, Watanabe T, Ito H, Watanabe S, Goto H, Gao P, Hughes M, Perez DR, Donis R, Hoffmann E, Hobom G, Kawaoka Y.** 1999. Generation of influenza A viruses entirely from cloned cDNAs. Proceedings of the National Academy of Sciences of the United States of America **96:** 9345-9350.

21. **Satoh H, Ueda T, Kobatake Y.** 1985. Oscillations in cell shape and size during locomotion and in contractile activities of Physarum polycephalum, Dictyostelium discoideum, Amoeba proteus and macrophages. Experimental Cell Research **156:** 79-90.

22. **Nayak DP, Hui EK, Barman S.** 2004. Assembly and budding of influenza virus. Virus Research **106:** 147-165.

23. **Rodriguez Boulan E, Sabatini DD.** 1978. Asymmetric budding of viruses in epithelial monlayers: a model system for study of epithelial polarity. Proceedings of the National Academy of Sciences of the United States of America **75:** 5071-5075.

24. **Le Ru A, Jacob D, Transfiguracion J, Ansorge S, Henry O, Kamen AA.** 2010. Scalable production of influenza virus in HEK-293 cells for efficient vaccine manufacturing. Vaccine **28:** 3661-3671.

25. **Bozzola JJ, Russell LD.** 1998. The mechanism of chemical fixation, p. 20-22. *In* B. L. McKean (ed.), Electron Microscopy, 2nd. Jones and Bartlett Publishers Inc., Massachusetts.

26. **Burleigh LM, Calder LJ, Skehel JJ, Steinhauer DA.** 2005. Influenza a viruses with mutations in the m1 helix six domain display a wide variety of morphological phenotypes. Journal of Virology **79:** 1262-1270.

27. **Harris A, Forouhar F, Qiu S, Sha B, Luo M.** 2001. The crystal structure of the influenza matrix protein M1 at neutral pH: M1-M1 protein interfaces can rotate in the oligomeric structures of M1. Virology **289:** 34-44.

28. **Chen BJ, Leser GP, Jackson D, Lamb RA.** 2008. The influenza virus M2 protein cytoplasmic tail interacts with the M1 protein and influences virus assembly at the site of virus budding. Journal of Virology **82:** 10059-10070.

29. **Booy FP, Ruigrok RW, van Bruggen EF.** 1985. Electron microscopy of influenza virus. A comparison of negatively stained and ice-embedded particles. Journal of Molecular Biology **184:** 667-676.

30. **Fujiyoshi Y, Kume NP, Sakata K, Sato SB.** 1994. Fine structure of influenza A virus observed by electron cryo-microscopy. EMBO Journal **13:** 318-326.

31. **Harris A, Cardone G, Winkler DC, Heymann JB, Brecher M, White JM, Steven AC.** 2006. Influenza virus pleiomorphy characterized by cryoelectron

tomography. Proceedings of the National Academy of Sciences of the United States of America **103:** 19123-19127.

32. **Baudin F, Bach C, Cusack S, Ruigrok RW.** 1994. Structure of influenza virus RNP. I. Influenza virus nucleoprotein melts secondary structure in panhandle RNA and exposes the bases to the solvent. EMBO Journal **13:** 3158-3165.

33. **Compans RW, Content J, Duesberg PH.** 1972. Structure of the ribonucleoprotein of influenza virus. Journal of Virology **10:** 795-800.

34. **Desselberger U, Racaniello VR, Zazra JJ, Palese P.** 1980. The 3' and 5'-terminal sequences of influenza A, B and C virus RNA segments are highly conserved and show partial inverted complementarity. Gene **8:** 315-328.

35. **Klumpp K, Ruigrok RW, Baudin F.** 1997. Roles of the influenza virus polymerase and nucleoprotein in forming a functional RNP structure. EMBO Journal **16:** 1248-1257.

36. **Tiley LS, Hagen M, Matthews JT, Krystal M.** 1994. Sequence-specific binding of the influenza virus RNA polymerase to sequences located at the 5' ends of the viral RNAs. Journal of Virology **68:** 5108-5116.

37. **Fodor E, Seong BL, Brownlee GG.** 1993. Photochemical cross-linking of influenza A polymerase to its virion RNA promoter defines a polymerase binding site at residues 9 to 12 of the promoter. Journal of General Virology **74 (Pt 7):** 1327-1333.

38. **Honda A, Ueda K, Nagata K, Ishihama A.** 1987. Identification of the RNA polymerase-binding site on genome RNA of influenza virus. Journal of Biochemistry **102:** 1241-1249.

39. **Murti KG, Webster RG, Jones IM.** 1988. Localization of RNA polymerases on influenza viral ribonucleoproteins by immunogold labeling. Virology **164:** 562-566.

40. **Schreier E, Ladhoff AM, Stompor S, Michel S.** 1988. Interaction between anti-influenza viral polymerase antibodies and RNP particles using the in vitro transcription process and an immunogold labelling technique. Acta Virologica **32:** 403-408.

41. **Arranz R, Coloma R, Chichon FJ, Conesa JJ, Carrascosa JL, Valpuesta JM, Ortin J, Martin-Benito J.** 2012. The structure of native influenza virion ribonucleoproteins. Science **338:** 1634-1637.

42. **Moeller A, Kirchdoerfer RN, Potter CS, Carragher B, Wilson IA.** 2012. Organization of the influenza virus replication machinery. Science **338:** 1631-1634.

43. **Chou YY, Vafabakhsh R, Doganay S, Gao Q, Ha T, Palese P.** 2012. One influenza virus particle packages eight unique viral RNAs as shown by FISH analysis. Proceedings of the National Academy of Sciences of the United States of America **109:** 9101-9106.

44. **Noda T, Sugita Y, Aoyama K, Hirase A, Kawakami E, Miyazawa A, Sagara H, Kawaoka Y.** 2012. Three-dimensional analysis of ribonucleoprotein complexes in influenza A virus. Nature Communications **3:** 639.

45. **Fournier E, Moules V, Essere B, Paillart JC, Sirbat JD, Cavalier A, Rolland JP, Thomas D, Lina B, Isel C, Marquet R.** 2012. Interaction network linking

the human H3N2 influenza A virus genomic RNA segments. Vaccine **30:** 7359-7367.

46. **Fournier E, Moules V, Essere B, Paillart JC, Sirbat JD, Isel C, Cavalier A, Rolland JP, Thomas D, Lina B, Marquet R.** 2012. A supramolecular assembly formed by influenza A virus genomic RNA segments. Nucleic Acids Research **40:** 2197-2209.

47. **R_Core_Team.** 2012. R: A language and environment for statistical computing. R Foundation for Statistical Computing, Vienna, Austria.

48. **Yakushevska AE, Lebbink MN, Geerts WJ, Spek L, van Donselaar EG, Jansen KA, Humbel BM, Post JA, Verkleij AJ, Koster AJ.** 2007. STEM tomography in cell biology. Journal of Structural Biology **159:** 381-391.

49. **Aoyama K, Takagi T, Hirase A, Miyazawa A.** 2008. STEM tomography for thick biological specimens. Ultramicroscopy **109:** 70-80.

50. **Ruigrok RW, Baudin F.** 1995. Structure of influenza virus ribonucleoprotein particles. II. Purified RNA-free influenza virus ribonucleoprotein forms structures that are indistinguishable from the intact influenza virus ribonucleoprotein particles. Journal of General Virology **76 (Pt 4):** 1009-1014.

51. **Torreira E, Schoehn G, Fernandez Y, Jorba N, Ruigrok RW, Cusack S, Ortin J, Llorca O.** 2007. Three-dimensional model for the isolated recombinant influenza virus polymerase heterotrimer. Nucleic Acids Research **35:** 3774-3783.

52. **Coloma R, Valpuesta JM, Arranz R, Carrascosa JL, Ortin J, Martin-Benito J.** 2009. The structure of a biologically active influenza virus ribonucleoprotein complex. PLoS Pathogens **5:** e1000491.

53. **Inglis SC, Carroll AR, Lamb RA, Mahy BW.** 1976. Polypeptides specified by the influenza virus genome I. Evidence for eight distinct gene products specified by fowl plague virus. Virology **74:** 489-503.

54. **Sugita Y, Noda T, Sagara H, Kawaoka Y.** 2011. Ultracentrifugation deforms unfixed influenza A virions. Journal of General Virology **92:** 2485-2493.

55. **Parvin JD, Palese P, Honda A, Ishihama A, Krystal M.** 1989. Promoter analysis of influenza virus RNA polymerase. Journal of Virology **63:** 5142-5152.

56. **Noda T, Kawaoka Y.** 2012. Packaging of influenza virus genome: robustness of selection. Proceedings of the National Academy of Sciences of the United States of America **109:** 8797-8798.

57. **Fujii Y, Goto H, Watanabe T, Yoshida T, Kawaoka Y.** 2003. Selective incorporation of influenza virus RNA segments into virions. Proceedings of the National Academy of Sciences of the United States of America **100:** 2002-2007.

58. **Hutchinson EC, von Kirchbach JC, Gog JR, Digard P.** 2010. Genome packaging in influenza A virus. Journal of General Virology **91:** 313-328.

59. **Muramoto Y, Takada A, Fujii K, Noda T, Iwatsuki-Horimoto K, Watanabe S, Horimoto T, Kida H, Kawaoka Y.** 2006. Hierarchy among viral RNA (vRNA) segments in their role in vRNA incorporation into influenza A virions. Journal of Virology **80:** 2318-2325.

60. **Gao Q, Brydon EW, Palese P.** 2008. A seven-segmented influenza A virus expressing the influenza C virus glycoprotein HEF. Journal of Virology **82:** 6419-6426.

61. **Gao Q, Chou YY, Doganay S, Vafabakhsh R, Ha T, Palese P.** 2012. The influenza A virus PB2, PA, NP, and M segments play a pivotal role during genome packaging. Journal of Virology **86:** 7043-7051.

62. **Mosley VM, Wyckoff RW.** 1946. Election micrography of the virus of influenza. Nature **157:** 263.

63. **Williams RC, Wyckoff RW.** 1945. Electron Shadow Micrography of the Tobacco Mosaic Virus Protein. Science **101:** 594-596.